



## RESEARCH ARTICLE

10.1002/2017JD027161

## Global Land Surface Temperature From the Along-Track Scanning Radiometers

D. J. Ghent<sup>1</sup> , G. K. Corlett<sup>1</sup> , F.-M. Göttsche<sup>2</sup> , and J. J. Remedios<sup>1</sup> <sup>1</sup>National Centre for Earth Observation, Department of Physics and Astronomy, University of Leicester, Leicester, UK, <sup>2</sup>Karlsruhe Institute of Technology, Eggenstein-Leopoldshafen, Germany

## Key Points:

- Presentation of the state-of-the-art Leicester ATSR and SLSTR Processor for LAnd Surface Temperature (LASPLAST)
- AATSR LST product with improved data provenance: better accuracy, fully traceable retrieval coefficients, and quantified uncertainty
- Validation of the AATSR LST data against in situ measurements acquired from 10 “gold standard reference” stations shows low bias

## Correspondence to:

D. J. Ghent,  
djg20@le.ac.uk

## Citation:

Ghent, D. J., Corlett, G. K., Göttsche, F.-M., & Remedios, J. J. (2017). Global land surface temperature from the Along-Track Scanning Radiometers. *Journal of Geophysical Research: Atmospheres*, 122, 12,167–12,193. <https://doi.org/10.1002/2017JD027161>

Received 18 MAY 2017

Accepted 31 OCT 2017

Accepted article online 3 NOV 2017

Published online 22 NOV 2017

**Abstract** The Leicester Along-Track Scanning Radiometer (ATSR) and Sea and Land Surface Temperature Radiometer (SLSTR) Processor for LAnd Surface Temperature (LASPLAST) provides global land surface temperature (LST) products from thermal infrared radiance data. In this paper, the state-of-the-art version of LASPLAST, as deployed in the GlobTemperature project, is described and applied to data from the Advanced Along-Track Scanning Radiometer (AATSR). The LASPLAST retrieval formulation for LST is a nadir-only, two-channel, split-window algorithm, based on biome classification, fractional vegetation, and across-track water vapor dependences. It incorporates globally robust retrieval coefficients derived using highly sampled atmosphere profiles. LASPLAST benefits from appropriate spatial resolution auxiliary information and a new probabilistic-based cloud flagging algorithm. For the first time for a satellite-derived LST product, pixel-level uncertainties characterized in terms of random, locally correlated, and systematic components are provided. The new GlobTemperature GT\_ATS\_2P Version 1.0 product has been validated for 1 year of AATSR data (2009) against in situ measurements acquired from “gold standard reference” stations: Gobabeb, Namibia, and Evora, Portugal; seven Surface Radiation Budget stations, and the Atmospheric Radiation Measurement station at Southern Great Plains. These data show average absolute biases for the GT\_ATS\_2P Version 1.0 product of 1.00 K in the daytime and 1.08 K in the nighttime. The improvements in data provenance including better accuracy, fully traceable retrieval coefficients, quantified uncertainty, and more detailed information in the new harmonized format of the GT\_ATS\_2P product will allow for more significant exploitation of the historical LST data record from the ATSRs and a valuable near-real-time service from the Sea and Land Surface Temperature Radiometers (SLSTRs).

## 1. Introduction

Land surface temperature (LST) as measured by ground-based, airborne, and spaceborne remote sensing instruments is the mean radiative skin temperature of all objects comprising the surface and provides the best approximation to the thermodynamic temperature based on a measure of radiance (Norman & Becker, 1995). Knowledge of LST is critical for numerous applications (Anderson et al., 2007; Anderson et al., 2011; Jin, Dickinson, & Vogelmann, 1997; Moran, 2003; Rhoads et al., 2001).

In the thermal infrared (TIR) atmospheric window (8–14  $\mu\text{m}$ ), the calibrated at-sensor radiance is dependent on both the true surface temperature and the surface emissivity, according to Planck's law. Through the inversion of Planck's law, LST can be estimated from satellite measurements of top-of-atmosphere (TOA) radiances as the radiative energy emitted by the surface is then directly related its temperature, although effects from surface emissivity and the atmosphere must also be considered. The principles of LST radiative transfer and algorithms have been established by a number of studies, including those of McMillin (1975) and Li and Becker (1993). However, recent years has seen considerable evolution as discussed in the review of Li et al. (2013) and in particular drivers toward globally applicable algorithms for long-term (climate-quality) data sets, detailed uncertainty analysis and cloud detection through improved radiative transfer simulations (Merchant et al., 2013).

The Along Track Scanning Radiometers (ATSRs) (Llewellyn-Jones & Remedios, 2012, and references therein) represent a niche type of sensor for climate data, incorporating conical scanning, dual views of each image pixel on the surface, precise thermal control of the instrument, and accurate radiometry. Sea surface temperature data sets from the ATSRs (Merchant et al., 2012; Veal et al., 2013), with uncertainty analysis, have provided records with stability of within 0.005 K/yr. AATSR on board the European Space Agency (ESA) Sun-synchronous, polar-orbiting satellite, Envisat, which was launched in March 2002, was the third in the

©2017. The Authors.

This is an open access article under the terms of the Creative Commons Attribution License, which permits use, distribution and reproduction in any medium, provided the original work is properly cited.

**Table 1**

*Main Characteristics of the Advanced Along-Track Scanning Radiometer (AATSR) and Sea and Land Surface Temperature Radiometer (SLSTR)*

	AATSR	SLSTR	
Swath width	500 km	1,420 km (nadir) 750 km (backward)	
Spatial sampling	1 km	500 m (visible, shortwave infrared) 1 km (medium wavelength infrared, TIR)	
Channels	Central wavelength (μm)	Bandwidth (μm)	Application
	0.555	0.02	Chlorophyll
	0.659	0.02	Vegetation index
	0.865	0.02	Vegetation index
	1.375 <sup>a</sup>	0.015	Cirrus detection
	1.615	0.06	Cloud clearing
	2.255 <sup>a</sup>	0.05	Cloud clearing
	3.740	0.38	Surface temperature
	10.85	0.90	Surface temperature
	12.00	1.00	Surface temperature

<sup>a</sup>Spectral channels are additional channels on SLSTR.

Along-Track Scanning Radiometer (ATSR) series of instruments (ATSR-1, ATSR-2, and AATSR). Data were acquired from AATSR until the failure of the Envisat platform on 8 April 2012. Continuity of the ATSR series is through the Sea and Land Surface Temperature Radiometer (SLSTR) on board the Sentinel 3 satellites, the first of which, Sentinel 3A, was launched on 16 February 2016. Table 1 introduces the main characteristics of both the AASTR and SLSTR instruments.

Several features make these instruments an important potential source of data for climate time series analysis of LST. First, these sensors have been designed to achieve high accuracies for the thermal channels through a highly stable in-flight calibration scheme. For ATSR-2 and AATSR thermometry and emissivity drift of the two onboard, calibration blackbodies have been less than 0.02 K over their respective operating periods (Smith, 2012). Second, the orbits of these satellites have been precisely controlled. Changes in local solar time of observations due to satellite orbital drift can introduce significant variations in observed LST because of diurnal variability (Gleason et al., 2002; Privette et al., 1995). Third, a low range of satellite viewing angles (maximum of 21° due to 512 km swath width) limit the impact on the LST record from directionality given the high spatial heterogeneity of the land surface (Ermdida et al., 2014, 2017; Pinheiro, Privette, & Guillevic, 2006; Vinnikov et al., 2012).

The purpose of this paper is to present the current version of what is now the Leicester ATSR and SLSTR Processor for LAnd Surface Temperature (LASPLAST) and the latest global LST product at 1 km produced for AATSR (GT\_ATS\_2P Version 1.0). First, we present an overview of the LASPLAST framework (section 2) including descriptions of the retrieval algorithm, input data sets, derivation of retrieval coefficients, cloud clearing scheme, and output data. Section 3 summarizes the uncertainty model applied to the AATSR data. In section 4, results of the validation of the GT\_ATS\_2P product against in situ LST are presented and compared with respect to the validation of the current ESA-operational AATSR LST product (ESA\_LST\_2P). These two products are also intercompared with a reference product. The main conclusions are summarized in section 5. Although not included in this paper, the intention is to apply the processor to ATSR-2 with similar quality and also, in a refined form, to SLSTR in the future.

LASPLAST uses a physics-based split-window retrieval approach that is near independent of in situ data (Prata, 1993, 1994, 2002). A new set of retrieval coefficients and across-track parameters have been generated for use with higher-resolution auxiliary data. Following the third reprocessing of ATSR data, LASPLAST has produced AATSR LST from the Level-1b brightness temperatures (BTs) in version 2.1 of the ATSR multi-mission archive ([http://browse.ceda.ac.uk/browse/neodc/aatsr\\_multimission](http://browse.ceda.ac.uk/browse/neodc/aatsr_multimission)). Other AATSR LST retrieval schemes have been developed (Coll et al., 2005; Soria & Sobrino, 2007) but are constrained to a regional deployment. The approach taken here is to develop retrieval coefficients that are both globally robust and fully traceable.

To complement the retrieval, theoretical pixel-level uncertainties have been quantified through an uncertainty model rather than through validation. A rigorous approach to uncertainty is taken using a

three-component model (random, locally correlated, and systematic), which considers how uncertainty is propagated. This is a necessary prerequisite for LST exploitation in land surface and climate models (Bosilovich et al., 2007; Ghent et al., 2010, 2011; Huang, Li, & Lu, 2008).

We also address the issue of cloud detection. The cloud detection scheme developed for use with LASPLAST determines the probability of clear-sky conditions for each pixel. Comparison against manually classified reference data has demonstrated (Bulgin et al., 2014) such an approach to be more accurate than static thresholds. Finally, retrievals over sea ice are a feature of LASPLAST.

## 2. Materials and Methods

This paper presents the features of LASPLAST as implemented in the GT\_ATS\_2P (version 1.0) product, which is available from ESA in the framework of the GlobTemperature project (<http://www.globtemperature.info/>) under the Data User Element of ESA's Fourth Earth Observation Envelope Programme (2013–2017). Four key features of LASPLAST are (i) globally robust retrieval coefficients, (ii) a model that calculates uncertainty on a pixel basis, (iii) higher-resolution auxiliary information, and (iv) a new probabilistic-based cloud discrimination algorithm. These features are important as they address limitations with early processing performed with the same Leicester retrieval algorithm (section 2.1) to produce the current ESA-operational product (ESA\_LST\_2P). These are well documented, arising as a result of unrepresentative coarse-resolution auxiliary information (Coll et al., 2012; Noyes, 2006, 2007) and cloud masking uncertainties. Nonetheless, retrieval accuracy of the ESA\_LST\_2P product has been shown to be better than 2.0 K (Coll et al., 2012; Noyes, 2007; Noyes, Soria, et al., 2007). This meets the product target accuracy (Llewellyn-Jones et al., 2001) of 2.5 K during the day but does not meet its intended 1.0 K target accuracy at night. Furthermore, the LST target accuracy for climate use in the 2016 Global Climate Observing System (GCOS) Implementation Plan (Global Climate Observing System (GCOS), 2016) is 1.0 K independent of day or night. The LASPLAST development is intended to progress further toward this ultimate goal.

### 2.1. Retrieval Algorithm

The most common approach to retrieve LST from space-based radiometers is the generalized split-window algorithm (Becker & Li, 1990; Wan & Dozier, 1996), which exploits differential absorption in two spectrally close TIR window channels for atmospheric correction and requires a priori knowledge of surface emissivity. This approach is implemented in some of the common operational products from satellite instruments such as the Moderate Resolution Imaging Spectroradiometer (MODIS) (Wan, 2008; Wan & Dozier, 1996) and the Spinning Enhanced Visible and InfraRed Imager (SEVIRI) (Freitas et al., 2010; Trigo et al., 2008). Essentially, algorithms utilize a set of retrieval coefficients that are applied to the brightness temperature (BT) data with dependences on emissivity and water vapor.

Whereas it is possible to retrieve temperature and emissivity simultaneously from TIR satellite sensors using a multichannel approach (Gillespie et al., 1998; Hulley & Hook, 2011), for two channels, the ill-posed problem is addressed using emissivity from an auxiliary data source. For AATSR, Soria and Sobrino (2007) performed a limited study of a range of algorithms at a local site, extended by Sobrino et al. (2016) to more sites for one algorithm. The former paper concentrated on water vapor and emissivity "explicit" algorithms and provided a framework in terms of assessing retrieval coefficient fitting error (model error), noise, emissivity, and water vapor errors. Sobrino et al. (2016) showed requirements for emissivity knowledge dynamically and showed good performance relative to ESA\_LST\_2P. We demonstrate superior performance for GT\_ATS\_2P relative to ESA\_LST\_2P.

The LASPLAST implementation use a nadir-only split-window algorithm that relies on statistics to generate realistic retrieval coefficients, with a defining feature a nonexplicit dependency on surface emissivity. Representative emissivities are folded into the coefficient fitting process on a per biome basis; uncertainties are generated in the fitting process and show reduced dependence on incomplete knowledge of surface emissivity. This is a useful approach since validation of dynamically varying emissivity remains challenging at scales appropriate to the pixel size. The LASPLAST approach proceeds via the following formulation (Prata, 2002):

$$LST = a_{f,i,pw} + b_{f,i}(T_{11} - T_{12})^n + (b_{f,i} + c_{f,i})T_{12} \quad (1)$$

where  $n = 1/(\cos(\theta/m))$  and  $m$  being a parameter controlling the dependence on view angle. The retrieval coefficients  $a_{f,i,pw}$ ,  $b_{f,i}$  and  $c_{f,i}$  are dependent on the biome ( $i$ ), fractional vegetation cover ( $f$ ), precipitable water ( $pw$ ), satellite zenith view angle ( $\theta$ ), and the time of day (day or night). The terms  $f$  and  $pw$  are seasonally dependent, whereas the biome ( $i$ ) is invariant. The retrieval coefficients  $a_{f,i,pw}$ ,  $b_{f,i}$  and  $c_{f,i}$  can further be partitioned into bare soil ( $b$ ;  $f = 0$ ) and fully vegetated ( $v$ ;  $f = 1$ ) components:

$$a_{f,i,pw} = d(\sec(\theta) - 1)pw + fa_{v,i} + (1 - f)a_{s,i} \quad (2)$$

$$b_{f,i} = fb_{v,i} + (1 - f)b_{s,i} \quad (3)$$

$$c_{f,i} = fc_{v,i} + (1 - f)c_{s,i} \quad (4)$$

where the six coefficients  $a_{v,i}$ ,  $a_{s,i}$ ,  $b_{v,i}$ ,  $b_{s,i}$ ,  $c_{v,i}$  and  $c_{s,i}$  are determined for each biome/time of day combination. The formulation of this algorithm means that land surface emissivity is dealt with implicitly through the radiative transfer simulation process to determine the coefficients. The inclusion of the parameter  $d$  accounts for the increase in atmospheric attenuation due to increased water vapor as the zenith viewing angle increases. For the GT\_ATS\_2P product the algorithm is applied over all land cover types and sea ice surfaces. Each surface type is represented by the biome classification. In the ESA\_LST\_2P product sea ice points were discarded through the land-sea mask. For the GT\_ATS\_2P product sea ice is treated as a common biome with land ice, i.e., utilizing the same retrieval coefficients. Identification of sea ice is described in section 2.2.4.

The algorithm introduces a weak nonlinearity in that the BT difference  $T_{11} - T_{12}$  varies by the power of  $n$ . The rationale is that the BT difference increases with increasing atmospheric water vapor, since attenuation due to water vapor is greater at  $12 \mu\text{m}$  than at  $11 \mu\text{m}$ . The inclusion of  $m$ , which is dependent on the zenith view angle, is supported by studies such as Coll and Caselles (1997) and Noyes (2007). While it is recognized that a LST algorithm with a nonlinear component for the BTs generally improves accuracy, there is an increase in sensitivity to uncertainties in emissivity (Wan & Dozier, 1996). This is greater though for algorithms with explicit emissivity.

While a characteristic of the ATSR instruments are the two (nadir and oblique) viewing angles, the LASPLAST only exploits observations in the nadir view. Potential exploitation of the oblique view for LST has received little attention, and where it has (Coll et al., 2006), the conclusion is that dual-angle algorithms are less accurate even over topographically flat and homogeneous surfaces, partly because of the differing sizes of the nadir and forward fields of view of the ATSR and partly because of uncertainties in pixel coregistration between the views.

## 2.2. Input Data Sets

The above discussion shows that the LASPLAST retrieval formulation is dependent on biome classification, fractional vegetation, and across-track water vapor dependences. The choice of these input data sets is critical to deliver products that can meet the 1.0 K LST target accuracy for climate (GCOS, 2016).

### 2.2.1. Biome

The biome data used in the GT\_ATS\_2P product is a variant of the 2006 Globcover product (Arino et al., 2007), which represents the mean state at approximately 300 m spatial resolution between December 2004 and June 2006 and is based on surface reflectance data from the Medium-Resolution Imaging Spectrometer. Other common operational LST products, such as MODIS and SEVIRI, have utilized land cover maps based on the International Geosphere-Biosphere Programme (IGBP) land cover classification. For the ESA\_LST\_2P product, the classification used employed 13 land biome classes and one lake class (Dorman & Sellers, 1989) at a coarse spatial resolution of  $0.5^\circ$ . The use of Globcover as a baseline in LASPLAST enables exploitation of the highest possible spatial resolution data set stratified into the highest number of classes. While IGBP may have an advantage of temporal variability, the variation in emissivity between biomes (Table 2) justifies the need for the increased stratification provided with Globcover.

Modifications to the Globcover product to meet the needs of the AATSR LST retrieval include (i) classification of permanent ice over Antarctica, which is missing in this Globcover version; (ii) distinction between inland/coastal water and open ocean; and (iii) partition of the single bare soil class into the most dominant soil types. The resultant ATSR Land Biome classification (ALB2) consists of 27 land and inland water/coastal water biomes and one open ocean biome (Table 2).

**Table 2**  
 ATSR LST Biome Classification Version 2 (ALB-2) Derived From the Globcover Classification

No.	Legend	Based on	11 $\mu\text{m}$ channel		12 $\mu\text{m}$ channel	
			$f = 0$	$f = 1$	$f = 0$	$f = 1$
0	Water bodies of sea (>10 km away from coast)	GC210 (GC0)	–	–	–	–
1	Postflooding or irrigated croplands	GC11	0.966	0.966	0.975	0.975
2	Rainfed croplands	GC14	0.970	0.971	0.979	0.976
3	Mosaic cropland (50–70%)/vegetation (grassland, shrubland, and forest) (20–50%)	GC20	0.969	0.960	0.971	0.971
4	Mosaic vegetation (grassland, shrubland, and forest) (50–70%)/cropland (20–50%)	GC30	0.966	0.961	0.966	0.971
5	Closed to open (>15%) broadleaved evergreen and/or semideciduous forest (>5 m)	GC40	0.971	0.961	0.972	0.972
6	Closed (>40%) broadleaved deciduous forest (>5 m)	GC50	0.973	0.969	0.974	0.972
7	Open (15–40%) broadleaved deciduous forest (>5 m)	GC60	0.961	0.959	0.959	0.971
8	Closed (>40%) needleleaved evergreen forest (>5 m)	GC70	0.975	0.967	0.974	0.969
9	Open (15–40%) needleleaved deciduous or evergreen forest (>5 m)	GC90	0.974	0.971	0.974	0.974
10	Closed to open (>15%) mixed broadleaved and needleleaved forest (>5 m)	GC100	0.973	0.971	0.972	0.973
11	Mosaic forest/shrubland (50–70%)/grassland (20–50%)	GC110	0.964	0.965	0.962	0.966
12	Mosaic grassland (50–70%)/forest/shrubland (20–50%)	GC120	0.967	0.961	0.967	0.966
13	Closed to open (>15%) shrubland (<5 m)	GC130	0.959	0.962	0.961	0.971
14	Closed to open (>15%) grassland	GC140	0.960	0.972	0.966	0.975
15	Sparse (>15%) vegetation (woody vegetation, shrubs, and grassland)	GC150	0.970	0.975	0.970	0.978
16	Closed (>40%) broadleaved forest regularly flooded—fresh water	GC160	0.970	0.957	0.974	0.970
17	Closed (>40%) broadleaved semideciduous and/or evergreen forest regularly flooded—saline water	GC170	0.969	0.959	0.971	0.972
18	Closed to open (>15%) vegetation (grassland, shrubland, and woody vegetation) on regularly flooded or waterlogged soil—fresh, brackish, or saline water	GC180	0.973	0.961	0.971	0.965
19	Artificial surfaces and associated areas (urban areas >50%)	GC190	0.962	0.972	0.970	0.978
20	Bare areas of soil types not contained in biomes 21–25	GC200 and other USDA soil types	0.954	0.980	0.970	0.943
21	Bare areas of soil type “Entisols-Orthents”	GC200/USDA-99	0.951	0.975	0.979	0.978
22	Bare areas of soil type “shifting sand”	GC200/USDA-1	0.949	0.982	0.972	0.984
23	Bare areas of soil type “Aridisols-Calcids”	GC200/USDA-55	0.948	0.982	0.970	0.984
24	Bare areas of soil type “Aridisols-Cambids”	GC200/USDA-56	0.950	0.961	0.970	0.959
25	Bare areas of soil type “Gelisols-Orthels”	GC200/USDA-7	0.969	0.969	0.972	0.973
26	Water bodies (inland lakes, rivers, and sea: max 10 km away from coast)	GC210	0.991	0.937	0.989	0.958
27	Permanent snow and ice	GC220 and ATSR land sea mask <60°S	0.988	0.988	0.981	0.981
28	No data (burnt areas, clouds, etc)	GC230	–	–	–	–

Note. Columns 4–7 detail emissivities calculated for each land and inland water biome (1–27) in the  $f = 0$  and  $f = 1$  cases for the 11 and 12  $\mu\text{m}$  channels from linear regression between CIMSS emissivities and corresponding fractional vegetation cover derived from the Copernicus global land service FCOVER product.

The ALB2 data set is made available to the LST retrieval at a spatial resolution of 1/120° (Figure 1) by regridding from the original 1/360° Globcover product based on the dominant biome or—if no biome is dominant—the center biome. For the distinction between inland/coastal water and open ocean the 1 km Naval Oceanographic Office data set (<https://www.ghrsst.org/data/ghrsst-data-tools/navo-ghrsst-pp-land-sea-mask/>) available from the Group for High Resolution Sea Surface Temperature is used, whereby all pixels greater than 10 km away from the coastline are classified as open ocean. The motivation for the partitioning of the single Globcover bare soil class into dominant soil types is to reduce the dispersion around bare soil mean emissivity. The partitioning criteria being that any soil type from the global soil map of the United States Department of Agriculture (Soil Survey Staff, 1999) with a coverage greater or equal to 0.5% of the global land surface is assigned to an additional biome class in the ALB2 classification. All remaining unclassified bare soil pixels are assigned to a generic “bare soil” class. Biomes are assigned to the AATSR pixels via a nearest neighbor approach.

### 2.2.2. Fractional Vegetation

For the GT\_ATS\_2P product the fractional vegetation cover ( $f$ ) is taken from the Copernicus Global Land Services FCOVER data set, which is available globally at 1/112° spatial resolution every 10 days from 1999 onward and acquired from a moving temporal window of approximately 30 days (Baret et al., 2013). The product covers the entire duration of the AATSR mission at the desired near 1 km resolution and assigned to the AATSR pixels via a nearest neighbor approach; ESA\_LST\_2P in contrast used the SiB/ISLSCP fractional

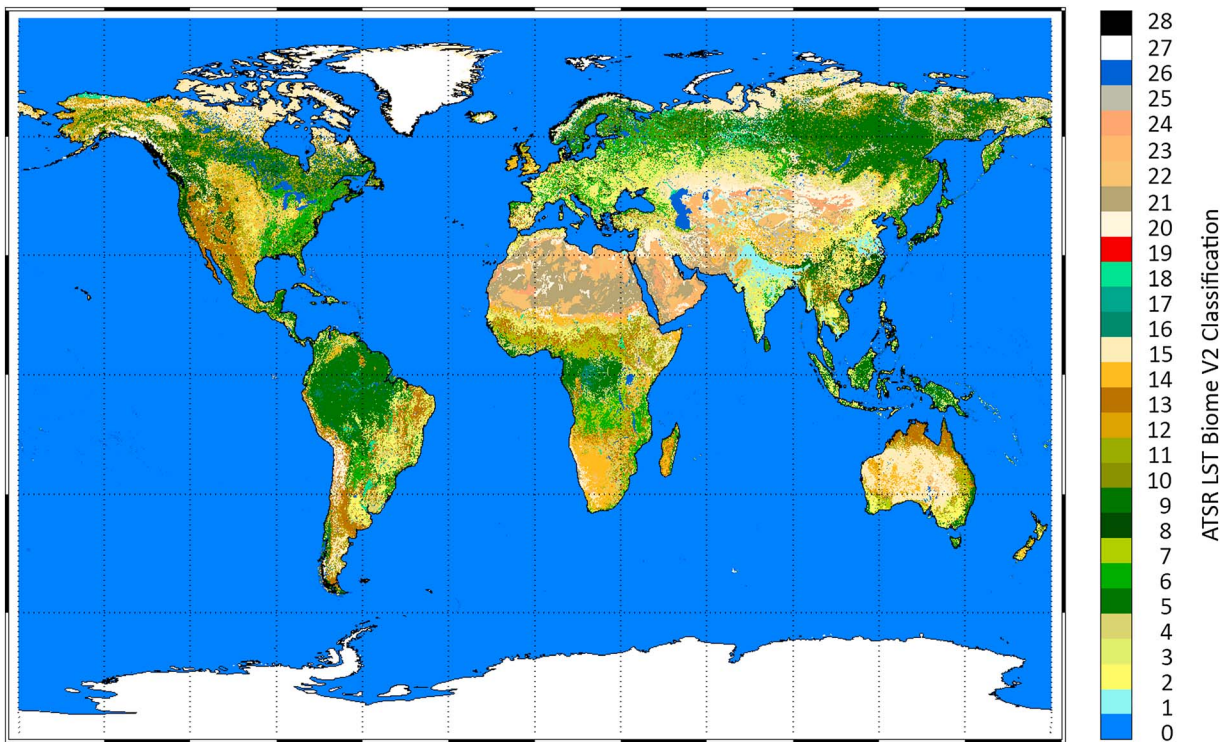


**Figure 1.** Global distribution of the ATSR LST biome version-2 (ALB-2) classes at 1/120° resolution.

vegetation cover product (Dorman & Sellers, 1989) at 0.5° and monthly averages. FCOVER is generated using a neural network trained with the 1-D radiative transfer models SAIL and PROSPECT as per Verger, Baret, and Camacho (2011), utilizing the normalized nadir reflectances in the red, near-infrared, and shortwave infrared wavebands of the VEGETATION instruments onboard SPOT-4 and SPOT-5. The validation of the product is described in Camacho et al. (2013), who conclude that the product shows good quality with a spatially consistent global distribution of retrievals. The comparison with ground measurements shows a root-mean-square error (RMSE) of 0.095.

For any pixel where no FCOVER value exists for a given 10 day window, either through missing data or poor quality, the pixel is filled if possible from climatology constructed for the same 10 day period across the AATSR period of 2002 to 2012. Data values range from 0.0 (no vegetation) to 1.0 (full vegetation). Grid cells flagged as snow or water are given the value 0.0.

### 2.2.3. Precipitable Water

The GT\_ATS\_2P retrieval uses precipitable water (pw) from the European Centre for Medium-Range Weather Forecasts (ECMWF) ERA-Interim reanalysis (Dee et al., 2011). The spatial resolution of approximately 0.7° is slightly coarser than the pw data set used in the ESA\_LST\_2P product (monthly averages at 0.5° derived from the NASA Water Vapor Project (NVAP) climatology (Randel et al., 1996)). Justification for this choice is detailed in Prata (2011), who argues that a change in spatial resolution is not significant for the retrieval algorithm. Rather, any spatial degradation is outweighed by the benefit gained from an increased temporal resolution.

Each precipitable water auxiliary data file is derived from 6-hourly monthly climatology corresponding to the four synoptic times—00UTC, 06UTC, 12UTC, and 18UTC—covering the 10 year period 2002–2011 inclusive. For each AATSR pixel, the value of pw is calculated through bilinear interpolation between the four surrounding pw values on the ERA-Interim grid extracted from the auxiliary data set and interpolated in time between the nearest two 6-hourly data. This is more coincident with the AATSR mission than the monthly files based on NVAP data for 1988–1992.

### 2.2.4. Surface Classification

The AATSR LST retrieval requires prior knowledge of the surface type to apply the most appropriate retrieval coefficients. Biome seasonality is described through change in fractional vegetation cover; additional cover

changes occur through changes in transient snow/ice cover. Where a pixel is identified as transient snow/ice, the LST retrieval for the GT\_ATS\_2P product applies the appropriate coefficients for snow/ice; ESA\_LST\_2P did not account for dynamic changes.

Over ocean the Operational Sea Surface Temperature and Sea Ice Analysis (OSTIA) daily sea ice analysis (Donlon et al., 2012) is used to identify snow/ice pixels. The OSTIA system is a daily global gap-free data set that includes sea ice area fraction produced on a  $0.05^\circ$  equal angle grid. The sea ice concentration, defined as the local area fraction of a given grid point that is covered by ice, is derived from passive microwave satellite measurements. The required sea ice concentration at  $1/120^\circ$  is produced by interpolating the input OSTIA data onto the ALB2 grid. Pixels with sea ice concentrations greater than 50% are designated as sea ice.

For Northern Hemisphere landmasses we use the daily Northern Hemisphere Interactive Multisensor Snow and Ice Mapping System (IMS) snow data set (Ramsey, 1998). This is produced on an equal area polar stereographic grid at a nominal resolution of 24 km and is available from 1997 onward. It is derived from a combination of satellite imagery, automated snow mapping algorithms, and other ancillary data. Here we regrid the IMS data to a resolution of  $1/120^\circ$  through nearest neighbor interpolation of the input IMS data.

In the Southern Hemisphere IMS data are not available, so transient snow/ice is identified through an approach based on the combined methods of Istomina et al. (2010) and Eastwood & Andersen (2007), which exploit all seven AATSR channels (visible and thermal) to produce a snow/cloud clearing mask and is superior to use of either method independently (Veal, personal communication). The approach attempts to account for the many factors that can affect the spectral signature of snow, such as atmospheric aerosol, ground contamination, and snow grain size—setting criteria to describe the spectral shape of snow. The criteria for the visible and near-infrared channels screen optically thick warm clouds but have difficulty with cirrus and optically thin clouds as they do not significantly modify the spectral signature of snow in those spectral regions; therefore, the TIR channels provide the necessary additional screening in these cases.

The IMS data set can provide a more robust generalized approach, whereas the combined algorithm is dependent on thermal IR data alone at night (Veal, personal communication). The necessary implication being that the uncertainty in the transient snow masking is greater in the Southern Hemisphere, although this is not quantified here.

### 2.3. Traceable Retrieval Coefficients

Globally robust retrieval coefficients have been generated to match the higher-resolution auxiliary data used in the GT\_ATS\_2P product. The process summarized here provides full traceability to the simulation input data and is an integral component of LASPLAST. In the original processing used for the ESA\_LST\_2P product, coefficients were determined nontraceably using simulations based on in situ sites (Prata, 1994).

#### 2.3.1. Radiative Transfer Simulations and Retrieval Coefficient Fitting

Consideration of the thermal radiative transfer equation for monochromatic radiation emitted and reflected from an assumed homogeneous surface and received by a spaceborne radiometer should be the starting point for an algorithm to retrieve LST (Prata, 2002). The heritage of ATSR retrieval coefficients, both for LST and sea surface temperature (SST), has been to define them by radiative transfer modeling rather than through empirical techniques (Embury, Merchant, & Filipiak, 2012; Merchant et al., 1999; Prata, 2002; Zavody, Mutlow, & Llewellynjones, 1995). An advantage of this approach is independence from in situ measurements. This is an important criterion for the long-term objective of developing a climate-quality product.

In contrast to the limited simulation data set used for the Soria and Sobrino (2007) study and for ESA\_LST\_2P, a critical consideration for the LASPLAST implementation is for fast processing of sufficient numbers of profiles to adequately characterize the entire range of potential atmospheric states representative of each biome class. In order to achieve this objective, we employed RTTOV-10.2 (Radiative Transfer Model for TIROS Operational Vertical Sounder satellite), which is a fast model for nadir viewing passive infrared and microwave satellite radiometers, spectrometers, and interferometers (Hocking et al., 2011; Saunders et al., 2012). This model covers the infrared spectral range of 3–20  $\mu\text{m}$ , governed by the range of the line-by-line data set LBLRTMv11.1 (Clough et al., 2005) on which the RTTOV infrared coefficients are determined. The accuracy and precision of the forward model can be assessed by means of a comparison between simulated and observed TOA radiances for a selection of known atmospheric and surface states. Bias between RTTOV and

the full line-by-line Reference Forward Model (<http://www.atm.ox.ac.uk/RFM/>) has been shown to be less than 0.1 K for AATSR channels (Embury, Merchant, & Corlett, 2012; Merchant & Le Borgne, 2004).

Linear regression is applied to the simulated BTs and corresponding skin temperatures to generate the  $a$ ,  $b$ , and  $c$  retrieval coefficients for both cases  $f = 0$  and  $f = 1$  in equations (2) to (4). The required inputs are vertical atmospheric profiles of temperature, ozone, and water vapor; surface and near-surface conditions; surface emissivities; and specification of the spectral response functions of the instrument. The distribution of the input profiles needs to encompass the full range of atmospheres and surfaces encountered, while also being representative of the mean conditions. Selected humidity profiles must characterize the large variation in concentration in the midtroposphere and lower troposphere (400 mb to 800 mb), the drier concentrations around the tropopause ( $\sim 100$  mb), and the less variable concentrations in the radiatively stable stratosphere ( $> 80$  mb). To satisfy these requirements ECMWF ERA-Interim (Dee et al., 2011) daily and invariant fields are used to generate the necessary profile data for RTTOV-10.2. For the spatial sampling strategy a uniform random sampling distribution is used to select clear-sky profile data for each biome class. A total of 4,560 locations are randomly selected across the land and ice surfaces to capture the full range of surface types over all the latitude/longitude bands. A temporal sampling strategy is then applied to ensure a comprehensive intraannual and interannual coverage—specifically, profiles are selected from the 15th day of every month covering the years 2002 to 2011 inclusive. For each spatially sampled profile, the two profiles temporally closest to the day and night AATSR local overpass times are selected from the 6-hourly data set. In total, 547,200 profiles are utilized.

For the algorithm form described in equations (1) to (4), Prata (1994) showed that the coefficients generated through regression were significantly different for day and night cases justifying separate implementations in the algorithm formulation. In a mixed pixel of vegetation and bare soil, for instance, the high emissivity of the vegetation can dominate the surface emission, whereas during the day, emission from the soil surface, which is subject to strong solar absorption, can have the largest influence with shadowing effects also arising. Differences between day and night in  $T_{\text{skin}}$  versus  $T_{\text{air}}$ , for example, also support the implementation of separate retrieval coefficients. The thermal radiance observed at top of atmosphere is dependent in a quasi non-linear way on the thermal contrast between the surface ( $T_{\text{skin}}$ ) and the near-surface air temperature ( $T_{\text{air}}$ ). The effect is explained by Bauduin et al. (2017). Furthermore, we have compared the performance of the algorithm when the day and night coefficients are switched in the retrieval and see differences between LST simulated with the retrieval coefficients and input surface temperature to the coefficient fitting as a function of temperature.

This sampling strategy ensures necessary representativeness of the global atmosphere and surface states across seasons and years. The final selection provides sufficient distributions of profiles for each biome; the minimum number of profiles is 480 for biome 16. Examination of the day and night coefficient fitting through comparison between LST simulated with the retrieval coefficients and input surface temperature to the coefficient fitting as a function of temperature (Figure 2) shows variability by temperature but no systematic increase in mean difference with temperature change. This test database is a global set of independent profiles covering all possible land cover types and distributed across all latitude/longitude covering a full annual cycle to be able to capture the seasonality. The statistical sampling results in a weighting similar to the fractional area occupied by the biomes, except that we impose a minimum sample size for each biome for robust statistics. The standard deviation in the fitting is generally larger at higher temperatures, although this is likely in part to be due to lower sampling. For some biomes (such as 14 and 15, which represent grassland and sparse vegetation) increasing differences toward low temperatures may be explained as a result of incorrect biome assignment in locations that are affected by transient snow but not reassigned in the simulations. The common LSTs tend to be associated with a higher range of water vapor, which is principally the source of the differences, whereas both lower LSTs (over snow/ice) and higher LSTs (over hot deserts) correspond to profiles with lower water vapor. The average uncertainty from the fitting per biome is propagated in the product uncertainty. Users should note that this uncertainty is overestimated at cold temperature and underestimated at the highest temperatures for most biomes. Traceability for the coefficient generation is delivered by maintaining a database of the selected profiles, which can be used for reproducing the coefficients.

Emissivity values for each channel are also required for simulating TOA brightness temperatures with RTTOV. To generate the three coefficients ( $a$ ,  $b$ , and  $c$ ) in equations (2)–(4) for both  $f = 0$  and  $f = 1$ , the corresponding

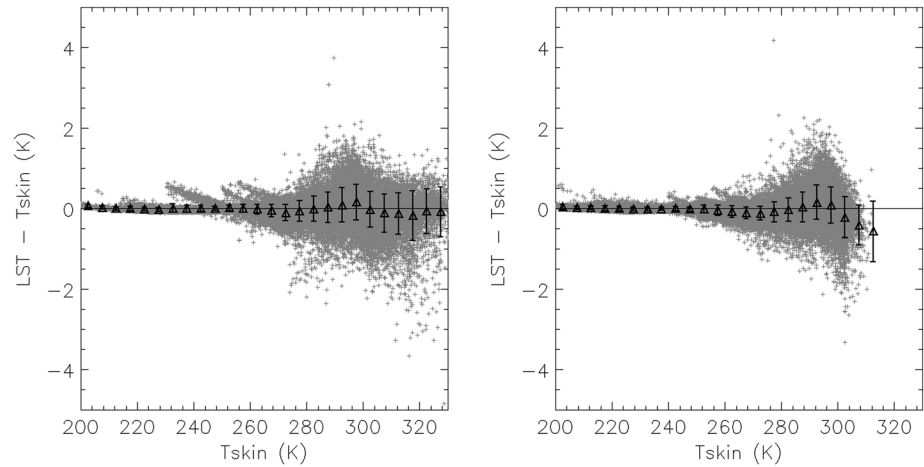


**Figure 2.** (left) Daytime and (right) nighttime differences as a function of temperature between LST simulated with the retrieval coefficients and input surface temperature to the coefficient fitting. Mean and standard deviations for each 5 K temperature band are shown.

emissivity estimates for both split-window channels for each biome have to be provided. For the simulations we use the Cooperative Institute for Meteorological Satellite Studies (CIMSS) global database of land surface emissivity (Seemann et al., 2008), which has been shown to generate accurate simulations of radiances over land (Koenig & de Coning, 2009). This data set is produced at a spatial resolution of 0.05° for 10 wavelengths between 3.6 μm and 14.3 μm representing hinge points, which capture most of the variation of the emissivity spectrum (Seemann et al., 2008). Assuming a linear relationship between emissivity and fractional vegetation cover, as in the Simplified NDVI<sup>THM</sup> (SNDVI<sup>THM</sup>) method for deriving emissivity (Sobrino et al., 2008), a linear regression technique is applied to fit CIMSS emissivities for the split-window channels to the fractional vegetation cover (*f*) auxiliary data:

$$\varepsilon_{\lambda} = \varepsilon_{v,\lambda}f + \varepsilon_{b,\lambda}(1 - f) \tag{5}$$

For each biome and channel the emissivity estimates for *f* = 0 and *f* = 1 (Table 2) are determined from the line of best fit for monthly emissivity and fractional vegetation matchups from 2 years (2007 and 2008) of data. Fitted mean emissivities from this approach for each biome are comparable to emissivities derived for similar land cover classes in the literature (Gottsche & Hulley, 2012; Hulley et al., 2009; Oltra-Carrio et al., 2012; Wan, 2008). For instance, values estimated here for the ALB2 classes are comparable with estimated values for similar IGBP classes (Peres & DaCamara, 2005). Taking the 11 μm channel as an example, ALB2 bare soil estimates range from 0.948 to 0.951 compared to a value of 0.948 for IGBP. For ice and water the ALB2 estimates are 0.988 and 0.991, respectively, with the corresponding values for IGBP being 0.989 and 0.990.

A further consideration in the determination of retrieval coefficients is the known offset to the AATSR 12 μm BT (Nightingale & Birks, 2004; O'Hara, 2013; Smith, 2014). We account for temperature-dependent differences in brightness temperature, which can range from 0.4 K for cold scene temperatures to −0.2 K for hot scenes, by applying the empirical nonlinearity correction to the measured 12 μm brightness temperatures in the Level-1b products taken from (Smith, 2014). An assessment of the absolute nadir residual bias is carried out, and an adjustment is made in the offset coefficients of the retrieval algorithm to correct for bias.

**2.3.2. Across-Track Model Fitting**

The AATSR nadir-only split-window LST algorithm (equation (1)) is designed to retrieve LST across track in a consistent manner. In the split-window retrieval, *T*<sub>11</sub> is less affected by atmospheric attenuation than *T*<sub>12</sub>. As the satellite zenith angle (SZA) increases from absolute nadir, the BT difference (*T*<sub>11</sub> − *T*<sub>12</sub>) increases due to the relatively larger increased attenuation in the 12 μm channel because of the increased absorption path length.

To assess the rationale for parameterizing the across-track retrievals for the GT\_ATS\_2P LST product, four realizations of the retrieval coefficients are compared: (i) absolute nadir coefficients and absolute nadir BT simulations (LST<sub>BT(0°),RC(0°)</sub>), (ii) absolute nadir coefficients and edge-of-swath BT simulations (LST<sub>BT(21°),RC(0°)</sub>),

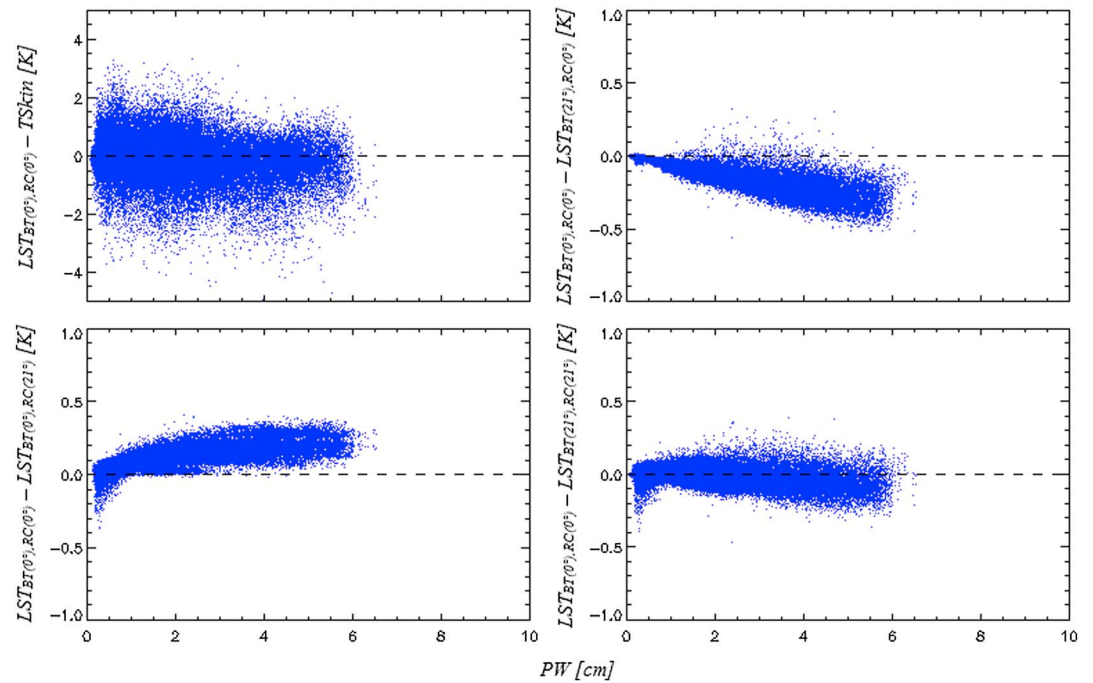


**Figure 3.** LST differences versus precipitable water for nadir swath retrievals: (top left)  $LST_{BT(0^{\circ}),RC(0^{\circ})} - T_{Skin}$  [K], where  $BT(0^{\circ})$  and  $RC(0^{\circ})$  refer to nadir swath simulated brightness temperatures and generated retrieval coefficients at absolute nadir ( $0^{\circ}$ ), respectively; (top right)  $LST_{BT(0^{\circ}),RC(0^{\circ})} - LST_{BT(21^{\circ}),RC(0^{\circ})}$ ; (bottom left)  $LST_{BT(0^{\circ}),RC(0^{\circ})} - LST_{BT(0^{\circ}),RC(21^{\circ})}$ ; (bottom right)  $LST_{BT(0^{\circ}),RC(0^{\circ})} - LST_{BT(21^{\circ}),RC(21^{\circ})}$ . For each scenario the baseline parameterization of  $m = 1$ , and  $d = 1$  in equations (1) and (2), respectively, is applied.

(iii) edge-of-swath coefficients and absolute nadir BT simulations ( $LST_{BT(0^{\circ}),RC(21^{\circ})}$ ), and (iv) edge-of-swath coefficients and edge-of-swath BT simulations ( $LST_{BT(21^{\circ}),RC(21^{\circ})}$ ). Each realization is analyzed with respect to precipitable water (Figure 3) where the nonlinear water vapor parameter  $d$  and the exponent  $n$  are both set equal to unity. The LST difference for  $LST_{BT(0^{\circ}),RC(0^{\circ})} - LST_{BT(21^{\circ}),RC(21^{\circ})}$  is minimized with a mean of  $-0.01$  K and a standard deviation of 0.05 K. In contrast, LST differences for  $LST_{BT(0^{\circ}),RC(0^{\circ})} - LST_{BT(21^{\circ}),RC(0^{\circ})}$  or  $LST_{BT(0^{\circ}),RC(0^{\circ})} - LST_{BT(0^{\circ}),RC(21^{\circ})}$  show increasing nonlinear negative or positive trends, respectively, as water vapor concentrations increase.

A common approach to account for such variability in operational products such as MODIS (Wan, 2008; Wan & Hulley, 2015) and SEVIRI (Freitas et al., 2010; Trigo et al., 2008) is to generate retrieval coefficients for different ranges of satellite zenith angle. The AATSR LASPLAST algorithm uses a single set of coefficients for the absolute nadir retrieval, and nonlinear water vapor and view angle sensitivities are instead parameterized. The offset term ( $d$  in equation (2)), which increases in an exponential fashion with increasing SZA, and the nonlinear adjustment to the brightness temperature difference ( $m$  in equation (1)) are iterated for each biome and diurnal state until the RMSE is minimized between ( $LST_{BT(0^{\circ}),RC(0^{\circ})}$ ) and ( $LST_{BT(21^{\circ}),RC(0^{\circ})}$ ). LST differences between two realizations (baseline retrieval and parameterized retrieval) are presented for each biome in Table 3. The differences in the response between surface types are minimal compared with the differences within a surface type as a function of increasing water vapor. This is to be expected since the difference between nadir and edge of swath for narrow swath instruments such as AATSR is dominated by the difference in atmospheric path length rather than surface emissivity anisotropy, which does not become significant until viewing angles increase above between  $30^{\circ}$  and  $40^{\circ}$  (Cuenca & Sobrino, 2004) beyond the range of AATSR. In almost all cases the RMSE has been substantially reduced through parameterization of  $d$  and  $m$ . The reductions range from 0.02 K for biome 25 (0.04 K to 0.02 K) to 0.29 K for biome 16 (0.37 K to 0.08 K).

#### 2.4. Cloud Clearing

A key improvement in the GT\_ATS\_2P product is the implementation of a cloud mask based on the probability of clear-sky conditions, which is a semi-Bayesian approach designated as UOL\_3. This approach uses

**Table 3**

Mean and Standard Deviations of LST Differences ( $LST_{BT(0^\circ),RC(0^\circ)} - LST_{BT(21^\circ),RC(0^\circ)}$ ) for Each Biome (1–27) and Diurnal State (Day or Night) for the Baseline Retrieval ( $d$  and  $m$  Both Unity) and the Parameterized Retrieval ( $d$  and  $m$  Parameterization)

ALB-2	Day				Night			
	Baseline retrieval		Parameterized retrieval		Baseline retrieval		Parameterized retrieval	
	$\mu$ ( $\Delta$ LST)	$\sigma$ ( $\Delta$ LST)	$\mu$ ( $\Delta$ LST)	$\sigma$ ( $\Delta$ LST)	$\mu$ ( $\Delta$ LST)	$\sigma$ ( $\Delta$ LST)	$\mu$ ( $\Delta$ LST)	$\sigma$ ( $\Delta$ LST)
1	0.149	0.027	-0.011	0.026	0.267	0.092	0.128	0.054
2	0.131	0.112	-0.062	0.010	0.190	0.082	0.085	0.049
3	0.208	0.040	-0.091	0.012	0.018	0.097	0.068	0.060
4	0.178	0.319	-0.106	0.122	0.181	0.072	0.076	0.046
5	0.294	0.022	0.041	0.022	0.385	0.057	0.126	0.058
6	0.120	0.038	-0.007	0.038	0.145	0.079	0.012	0.045
7	0.169	0.013	0.048	0.013	0.222	0.033	0.080	0.031
8	0.158	0.040	0.010	0.040	0.154	0.082	0.021	0.047
9	0.042	0.024	-0.008	0.023	0.033	0.046	-0.010	0.030
10	0.081	0.039	0.019	0.025	0.085	0.043	0.028	0.021
11	0.111	0.043	-0.005	0.041	0.131	0.071	0.007	0.034
12	0.105	0.025	0.040	0.025	0.101	0.066	0.032	0.039
13	0.099	0.015	-0.015	0.005	0.197	0.079	0.095	0.048
14	0.110	0.050	0.027	0.052	0.136	0.066	0.059	0.039
15	0.065	0.028	0.015	0.028	0.050	0.086	0.000	0.057
16	0.278	0.034	0.081	0.049	0.374	0.023	0.172	0.035
17	0.203	0.007	-0.074	0.096	0.277	0.047	0.039	0.068
18	0.102	0.050	0.029	0.039	0.119	0.096	0.026	0.051
19	0.139	0.048	0.018	0.054	0.148	0.058	0.019	0.046
20	0.094	0.043	0.008	0.043	0.119	0.074	0.025	0.039
21	0.108	0.030	0.019	0.053	0.158	0.030	0.069	0.028
22	0.133	0.031	0.004	0.053	0.180	0.060	0.045	0.037
23	0.141	0.028	0.008	0.056	0.159	0.050	0.045	0.028
24	0.102	0.019	0.021	0.044	0.141	0.051	0.061	0.031
25	0.038	0.022	0.006	0.017	0.035	0.035	0.002	0.019
26	0.093	0.093	0.018	0.064	0.120	0.071	0.040	0.033
27	0.014	0.002	0.014	0.002	0.006	0.002	0.006	0.002

Note. BT(0°) and BT(21°) refer to absolute nadir and edge-of-swath simulated brightness temperatures, respectively, and RC(0°) refers to absolute nadir generated retrieval coefficients.

atmospheric profile information to interpret clear-sky conditions for the coincident space and time of acquisition by the instrument. The coincidence is modeled through bilinear interpolation of surrounding profiles and temporal interpolation between 6-hourly analysis fields. On a spatial plane these modeled profile data correspond to AATSR orbit granules, which are orbit subsets of pixels every 25 km across track and 32 km along track. Geolocation information is available in the Level-1b data for the vertices (tie-points) of these granules. Using RTTOV, expected clear-sky brightness temperatures/brightness temperature differences (BTDs) are simulated for these profile data. Pixel information on clear-sky conditions within a granule are derived from probability density functions (pdf), in which a normal distribution is assumed. For each pdf, the mean is the simulated brightness temperature/BTD for the granule and the standard deviation is the observational climatology for the corresponding month, biome, and diurnal state. A per-pixel cloud mask is generated from comparing the pixel BTs/BTDs with the pixel pdfs. If the combined probabilities are less than a confidence threshold, the pixel is identified as cloudy.

The cloud detection approach used in the ESA\_LST\_2P product is that referred to as SADIST (Birks, 2007) based on the heritage of the Advanced Very High Resolution Radiometer Processing Over Land Cloud and Ocean cloud mask (Saunders, 1986). The threshold-based SADIST cloud detection scheme is based on static latitudinal based thresholds for different cloud types.

In a comparison of six different cloud detection schemes, including Bayesian, semi-Bayesian, and threshold-based, for AATSR against manually classified reference data (Bulgin et al., 2014), the UOL\_3 scheme exhibited the highest overall percentage of perfect (PP) classification (91.71%), and for all but the heaviest aerosol loading, the highest true skill scores (TSS) (77.93%). The corresponding statistics for the SADIST cloud detection

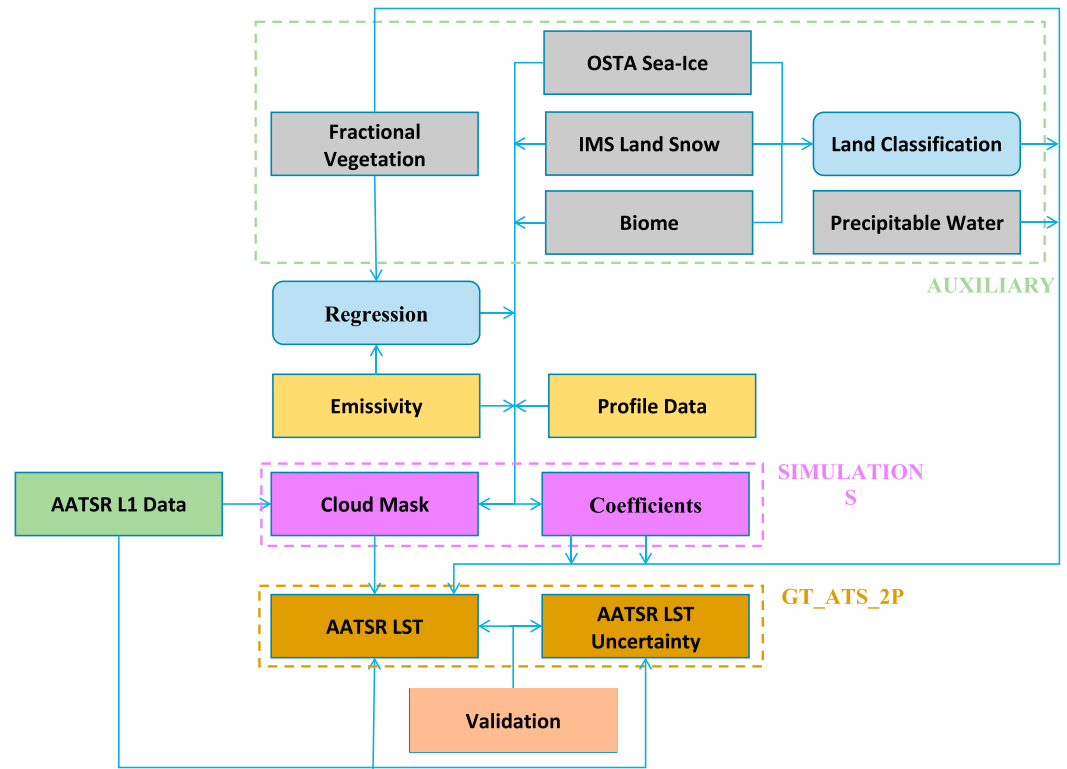


**Figure 4.** Illustration of the production of the GlobTemperature AATSR LST product (GT\_ATS\_2P) with the Leicester ATSR and SLSTR Processor for LAnd Surface Temperature (LASPLAST).

scheme (used in ESA\_LST\_2P) were 83.86% (PP) and TSS (69.27%), where PP is the percentage of all pixels correctly classified as either cloud or clear and TSS is the percentage of cloud pixels correctly identified minus the percentage of clear pixels erroneously flagged as cloud. These statistics were compiled from the performance of the algorithms under 21 different scenarios that were expertly classified. These covered different cloud types and cloud fragmentation over multiple surfaces. This study provides clear evidence that the cloud detection in GT\_ATS\_2P (UOL\_V3 scheme) consistently outperforms the cloud detection in ESA\_LST\_2P (SADIST scheme) under different clear-sky and cloud conditions. Work to further validate different cloud masks is being carried out in GlobTemperature. The UOL\_3 scheme is equally robust for both day and night since it exploits only information in the thermal channels; in contrast, the SADIST scheme uses both the visible and thermal channels, and thus, only a subset of its cloud tests is used for nighttime retrievals.

**2.5. Outputs and Processor Overview**

Figure 4 summarizes the different components in the LASPLAST system relating to the GT\_ATS\_2P product. Version 1.0 of the GT\_ATS\_2P product is freely available on the GlobTemperature Data Portal (<http://data.globtemperature.info/>) in a format harmonized across all data streams disseminated. The harmonized format provides consistent standardized metadata across all LST products and a common data format, which is well established and internationally accepted by the user community. In addition to LST and accompanying uncertainty information, the Level-2 product contains data on geolocation, acquisition time, satellite viewing geometry, and quality, all at full resolution. Auxiliary data, such as dynamic biome, fractional vegetation, water vapor content, are also available. The LST uncertainty is provided both as a total value per pixel and per component as described in section 4. Figure 5 illustrates an example of the product content for a scene within one orbit.

GT\_ATS\_2P Level-2 data have been quality checked with regard to input Level 1b data, with only valid data stored. Surface temperature data are calculated over land (including ice sheets), lakes, and sea ice. No LST data are available over open ocean pixels. LST is derived for all valid pixels and made available in the

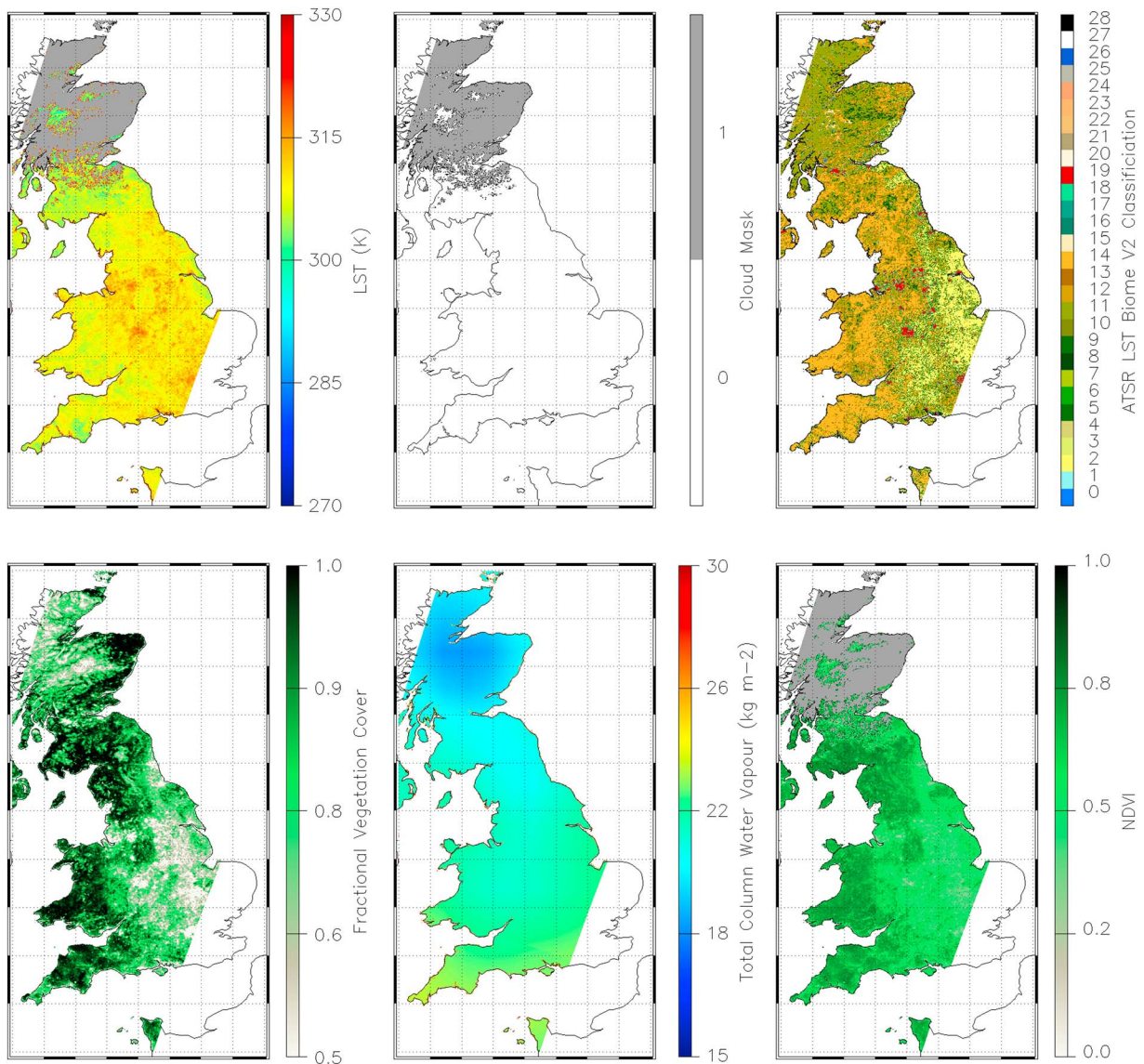


**Figure 5.** Example data available within the GT\_ATS\_2P product (GT\_SSD-L2-AATSR\_LST\_2-20060718\_102137-CUOL-0.01X0.01-http://v1.0.nc). Top row from left to right: LST; UOL\_V3 cloud mask; biome. Bottom row from left to right: fractional vegetation cover; precipitable water; NDVI.

output. The cloud clearing mask together with information on low confidence pixels and transient snow cover are also provided. Pixels masked as cloud contaminated or low confidence should not be used, and these masks should be applied when propagating the LST data to higher levels. An indication of the level of quality in the remaining pixels can be ascertained from the value of the LST uncertainty.

### 3. Uncertainty Model

The ESA\_LST\_2P product does not contain any information on the uncertainty of the LST data. Uncertainty represents the doubt on how well the result of the measurement represents the value of the quantity being measured. The lack of such metric reduces the meaningfulness of a product and of comparisons against reference values. In the LASPLAST implementation pixel-level uncertainties have been quantified through an uncertainty model. Previous attempts have been made to quantify the associated uncertainty of LST data (Freitas et al., 2010; Hulley, Hughes, & Hook, 2012; Jimenez-Munoz & Sobrino, 2008; Soria & Sobrino, 2007). While these share some features with the approach followed here, there is some inconsistency in how they are presented to the product users. A consistent approach to the definition of LST uncertainties is proposed

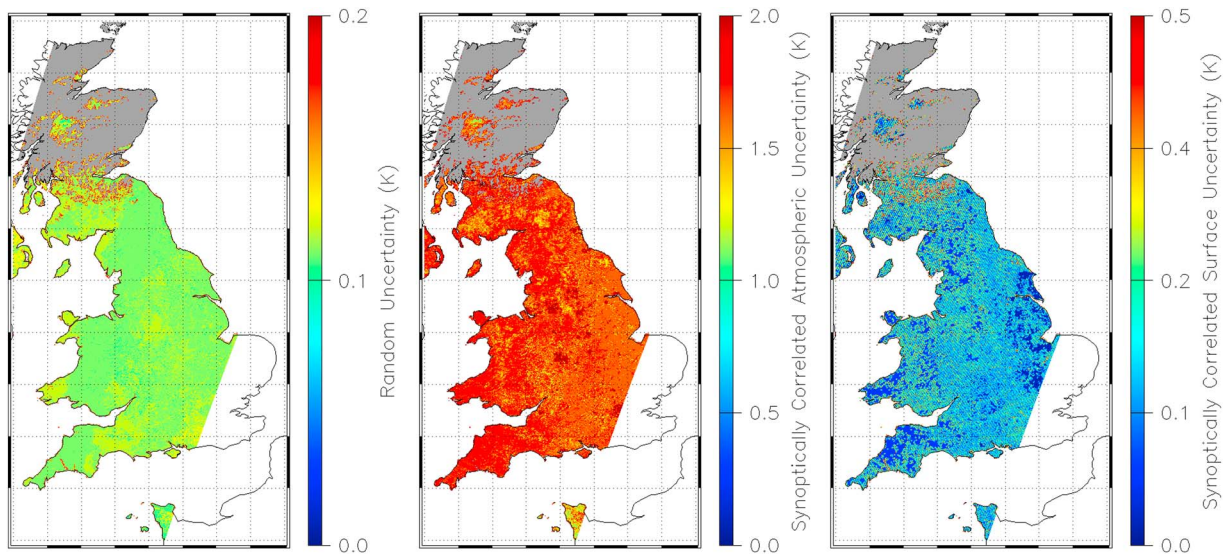


**Figure 6.** Pixel-level LST uncertainty budget of a typical orbit of AATSR data from the GT\_ATS\_2P product (GT\_SSD-L2-AATSR\_LST\_2-20060718\_102137-CUOL-0.01X0.01-http://v1.0.nc): (left) random component, (middle) locally correlated atmospheric component, and (right) locally correlated surface component.

here. This follows the concepts for sea surface temperature (Bulgin et al., 2016) and is equally applicable across surface temperature domains. Here we present an overview of this approach applied to AATSR data.

Generally, for each pixel, three components of uncertainty exist, representing the uncertainty from effects whose errors have distinct correlation properties: (i) random, (ii) locally correlated, and (iii) large-scale systematic. Random components are from effects whose errors between pixels are uncorrelated. Systematic components are from effects whose errors between pixels are correlated. Where these errors are correlated between nearby pixels they are categorized as locally correlated and are modeled via spatiotemporal correlation length scales. Errors that are correlated between distant pixels are categorized as large-scale systematic. Where a systematic error can be quantified in the analysis of a retrieval scheme this should be analyzed—and if possible—the retrieval algorithm corrected. The application of such an uncertainty approach to LST data represents a significant advance on what has generally been done for LST products to date and may help to identify algorithm strengths and weaknesses.

### 3.1. Random Uncertainties

The radiometric noise is a random component of the uncertainty budget, which is uncorrelated between individual pixels. The assumption is that the radiometric noise is sufficiently Gaussian and small so that the law of propagation of uncertainty is adequate for this propagation. The expected instrumental noise for the 11 and 12  $\mu\text{m}$  channels is taken from the typical respective noise equivalent differential temperatures ( $NE\Delta T$ ) for AATSR:  $NE\Delta T_{11} = NE\Delta T_{12} = 0.05$  K (Smith, 1999); note that per pixel values are not available in the AATSR level 1b data. The associated uncertainties in retrieved LST for each pixel are determined by multiplying these values with the respective partial derivatives of the retrieval algorithm (equation (1)) for  $T_{11}$  and  $T_{12}$  and combining the results in quadrature. Typical values of the estimate of uncertainty from random effects are illustrated in Figure 6 for an example orbit from the GT\_ATS\_2P product.

### 3.2. Locally Correlated Uncertainties

Locally correlated uncertainties in the GT\_ATS\_2P product represent the uncertainty due to errors in the atmospheric state, such as water vapor, and errors in surface parameters, such as emissivity variability within a biome and geolocation accuracy. The locally correlated component is split between the atmosphere and the surface on the basis of different correlation length scales.

For the radiative-transfer-based retrieval coefficients implemented in the GT\_ATS\_2P product, errors in atmospheric state are a prime contributor to the residuals of the fit, which generate retrieval coefficients. However, so also are variations in the input emissivities. An estimate of the combined atmospheric and emissivity

uncertainty component is the standard deviation of the differences between simulated-retrieved and simulated-input surface temperatures. Errors in water vapor are the main source of atmospheric uncertainty in the coefficient fitting. Recent studies suggest that water vapor may be correlated on spatiotemporal scales of up to a few kilometers and a few minutes (Steinke et al., 2015; Vogelmann et al., 2015). For each subset of retrieval coefficients (categorized by biome and diurnal state) the combined uncertainty component is estimated, stratified into 5° bands of satellite viewing angle to better parameterize the variations within the uncertainty model.

A further source of uncertainty from surface effects, whose errors are locally correlated, is fractional vegetation cover. This is analogous to variations in surface emissivity (Sobrino et al., 2008) and is assumed to have a correlation length scale related to the distribution of biomes. The error in the fractional vegetation cover input state is taken directly from the Copernicus Global Land Services FCOVER data set on a per pixel basis (Baret et al., 2013; Camacho et al., 2013). These errors are multiplied with the partial derivative of the LST retrieval algorithm (equation (1)) with respect to  $f$  for each pixel.

An additional source of uncertainty from effects whose errors are locally correlated with a length scale related to the distribution of biomes is geolocation. In effect this is an uncertainty in the assignment of the underlying biome, and thus an uncertainty in the parameterization of the retrieval. This uncertainty arises from two sources: (i) a correction of the known geolocation mismatch and (ii) the reprojection of native “instrument” pixels onto the “image” grid.

As a consequence of the conical scanning geometry of the AATSR instrument the native instrument pixels lie on a series of curves formed by the intersection of the scan cone with the surface of the Earth. During a regrid-ding stage of the processing the instrument pixels are reprojected onto the nearest quasi-Cartesian “image” grid points centered on the satellite ground track (Birks, 2010). A consistent offset in the absolute nadir geolocation between coincident AATSR BTs and biome classification in the Globcover data set (Zeller & Ghent, 2011) was implemented in the third ATSR reprocessing. However, the image data may still deviate by 0.5 km from the “true” instrument pixel coordinates (Zeller & Ghent, 2011). This uncertainty propagates to the LST retrieval algorithm via a pixel’s assigned biome and is estimated by determining the probability that the biome is correctly assigned.

For an estimated 0.5 km geolocation error, this assumes that the biome assigned to a pixel can be found within a  $3 \times 3$  pixel area centered on it. For each of the  $3 \times 3$  pixels distance is calculated with respect to the coordinates of the center pixel. Weights are calculated using an inverse distance weighting method as a measure of the probability of the biome classification being the true classification. The uncertainty is derived by multiplying these probabilities with estimated LST errors due to biome misclassification. These errors are obtained from differences between LST retrieved for the assigned biome and retrieval for each of the alternative biomes. Typical uncertainty estimates from locally correlated effects are shown in Figure 6 for the GT\_ATS\_2P product.

### 3.3. Large-Scale Systematic Uncertainties

Systematic uncertainty is introduced to the LST retrieval through two sources: (i) uncertainty in the calibration of the measuring instrument and (ii) uncertainty in the radiative transfer modeling to simulate the radiances for each instrument channel in the derivation of the retrieval coefficients. In the GT\_ATS\_2P product known bias in the instrument calibration is corrected for in the offset coefficients of the retrieval algorithm. In the absence of detailed knowledge of the calibration errors we assume any such residual biases to have a negligible impact on the LST product. Estimates of uncertainty in the radiative transfer modeling can be determined by repeating simulations with perturbations applied to a parameter of interest. For the AATSR 11  $\mu\text{m}$  channel these have been evaluated to be consistent to within 0.03 K (Embury, Merchant, & Corlett, 2012) and is used for both channels. These systematic uncertainties propagate through into the total LST retrieval uncertainty.

### 3.4. Other Unquantified Contributory Effects

For each pixel the calculated uncertainty estimate has assumed clear-sky conditions. This neglects the possibility that the retrieved LST for any given pixel may be subject to cloud contamination, but which has not been masked by the cloud detection scheme. The probability of such occurrences may be greater for cloud edges or for clouds that are sufficiently small or optically thin. One possibility to quantify such an uncertainty

**Table 4***Characteristics of the In Situ Stations of the SURFRAD Network and the ARM Southern Great Plains Site*

Site	Latitude	Longitude	Elevation	Surface type	Biome
Bondville	40.05155	−88.37325	230 m	Grassland	3
Desert Rock	36.62320	−116.01962	1007 m	Arid shrub land	13
Fort Peck	48.30798	−105.10177	634 m	Grassland	11
Goodwin Creek	34.2547	−89.8729	98 m	Grassland	11
Penn State University	40.72033	−77.93100	376 m	Cropland	3
Sioux Falls	43.73431	−96.62334	473 m	Grassland	14
Table Mountain	40.12557	−105.23775	1689 m	Sparse grassland	11
Southern Great Plains	36.605° N	97.485° W	318 m	Pasture/wheat/bare soil	2

may be to exploit simulated data to estimate an average impact on the LST of misclassification with the probability of any given pixel being misclassified derived from an assessment of the cloud masking scheme together with climatological knowledge of cloud distributions from the International Satellite Cloud Climatology Project (Rossow & Schiffer, 1999). At present though such a method is exploratory, and we have no robust method for including this in the uncertainty budget. Thus, the contribution of this effect to LST uncertainty remains for future evolution of LASPLAST.

A likely further source of uncertainty is any temperature dependency error outside the medium temperature range. This may be caused by either nonlinear behavior above and below the onboard blackbody temperatures or the statistical sampling of the profiles used in the coefficient fitting. Figure 2 captures the uncertainty from the fitting process as a function of temperature for day and night, respectively. The estimate of the combined atmospheric and emissivity uncertainty component from the fitting process presented in section 3.2 is an overall estimate per biome and day/night. Nevertheless, further analysis of both a temperature-dependent stratification of the uncertainty and any biome misclassification uncertainty will be performed for future evolutions of the LASPLAST products.

## 4. Product Assessment

### 4.1. Validation Against In Situ LST

Both the GT\_ATS\_2P and ESA\_LST\_2P products have been validated with high quality in situ observations from (i) two permanent validation stations managed by the Karlsruhe Institute of Technology (KIT), where routinely calibrated instrumentation is employed to measure radiometric temperatures (Gobabeb, Namibia and Evora, Portugal), and (ii) eight stations located in across the U.S. covering different surface and climatological conditions (Table 4)—seven SURFRAD (Surface Radiation Budget) network stations and one station from the ARM (Atmospheric Radiation Measurement) network. Gobabeb station (22.33°S, 15.03°E) is in a hot arid climate with an average annual precipitation less than 100 mm at an altitude of 408 m. The tower is situated on large gravel plains sparsely covered by desiccated grass covering an area of over 900 km<sup>2</sup>. A comprehensive description of Gobabeb station and the derivation of in situ LST are given in Gottsche, Olesen, and Bork-Unkelbach (2013) and Göttsche et al. (2016). The Evora site (38.54°N, 8.00°W) experiences a temperate Mediterranean climate, with a landscape of evergreen oak trees and grass; in situ LST is derived from a weighted average of the radiances of the two end-members (Ermida et al., 2014; Trigo et al., 2008). For the SURFRAD and ARM stations details of the instrumentation and calibration can be found in Augustine, DeLuisi, and Long (2000) and Morris (2006), respectively. These stations have become well established for validation of LST products in recent years (Li et al., 2014; Liu et al., 2015; Sobrino et al., 2016; Yu et al., 2012).

Figure 7 (top row) illustrates the validation of ESA\_LST\_2P (Figure 7, left column) and GT\_ATS\_2P (Figure 7, right column) for 2009 at Gobabeb separated into day and night matchups. The figure clearly shows that the mean difference to the in situ observations and their dispersion are higher for ESA\_LST\_2P than for GT\_ATS\_2P: the mean and standard deviations for ESA\_LST\_2P are −3.75 K and 1.30 K, respectively, whereas for GT\_ATS\_2P the corresponding statistics are −1.11 K and 1.14 K, respectively. Furthermore, when analyzing the temperature differences over time, the ESA\_LST\_2P data exhibit a distinct temperature-dependent pattern with generally positive differences for high temperatures (local summer) and negative differences for low temperatures (local winter), which is the case for day and night retrievals. Such a seasonal pattern was also found by Noyes et al. (2006) in their validation of AATSR over several Northern Hemisphere sites. The

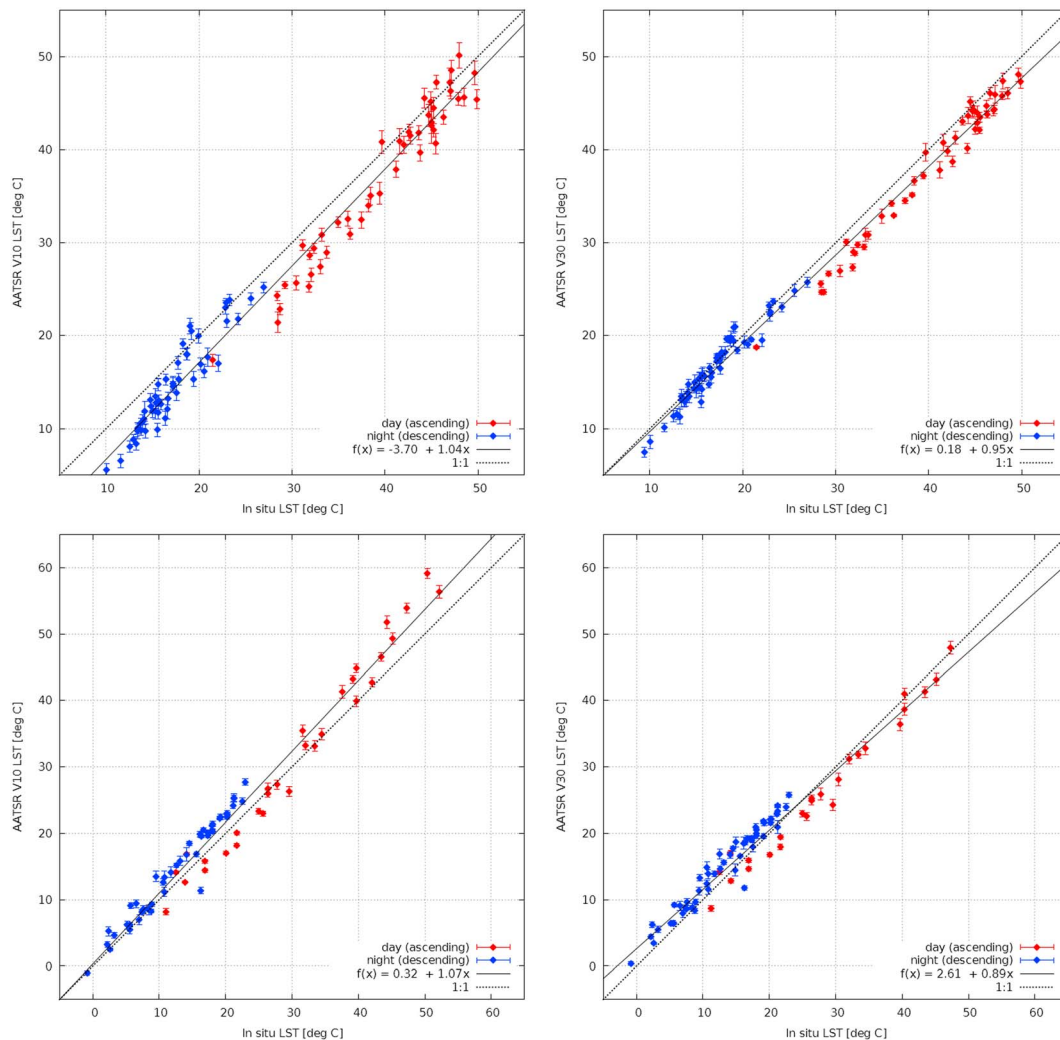


**Figure 7.** AATSR LST versus ground-based LST matchups for the KIT stations: (top row) Gobabeb and (bottom row) Evora during 2009 for both day (red) and night (blue). (left column) ESA\_LST\_2P matchups and (right column) GT\_ATS\_2P matchups.

sensitivities of the ESA\_LST\_2P retrieval algorithm to atmospheric water vapor, atmospheric temperature, and skin temperature were ascribed (Noyes, Corlett, et al., 2007) as the main reason for this so-called warm bias in local summer and cold bias in local winter. Temperature dependency in Figure 7 appears much reduced for GT\_ATS\_2P, demonstrating that the GT\_ATS\_2P retrieval coefficients are more representative of the full range of atmospheric states.

For validation of the 2009 data over the Evora site (Figure 7, bottom row) the GT\_ATS\_2P retrievals show good agreement with the in situ LST with low mean difference and standard deviation: 1.16 K and 1.40 K, respectively. For ESA\_LST\_2P the corresponding mean difference and standard deviation are 2.61 K and 1.66 K, respectively. For daytime retrievals, the difference between GT\_ATS\_2P and ESA\_LST\_2P matchups is larger than at night. Unlike at Gobabeb, which has a high degree of surface homogeneity, Evora LST is obtained from two principle end-members and the upscaling to satellite pixel scale introduces additional uncertainty (Kabsch, Olesen, & Prata, 2008; Trigo et al., 2008). The lower mean difference and standard deviation for GT\_ATS\_2P suggest that it is more robust than ESA\_LST\_2P to end-member cover fractions varying with viewing geometry. During the local summer when temperatures are higher and an inaccurate representation of the (hotter) grass background and the tree crown have greater impact, this is particularly important. Both at Gobabeb and Evora the validation of GT\_ATS\_2P is comparable with the performance of other common LST products (Ermida et al., 2014; Göttsche et al., 2016).

**Table 5**  
*In Situ Validation Statistics During 2009 for Both AATSR LST Retrievals (ESA\_LST\_2P and GT\_ATS\_2P) With Respect to the KIT Stations at Gobabeb and Evora, the Seven SURFRAD Sites, and One ARM Site*

Site	LST product	Day			Night		
		$\mu$ (K)	$\sigma$ (K)	RMSE (K)	$\mu$ (K)	$\sigma$ (K)	RMSE (K)
Gobabeb	ESA_LST_2P	-3.28	1.30	3.53	-4.11	1.13	4.26
	GT_ATS_2P	-2.41	0.81	2.54	-0.37	0.67	0.76
Evora	ESA_LST_2P	0.40	2.79	2.82	2.45	1.07	2.67
	GT_ATS_2P	-1.83	0.68	1.95	1.88	0.74	2.02
Bondville	ESA_LST_2P	0.88	1.74	1.95	1.03	1.43	1.76
	GT_ATS_2P	1.22	1.09	1.64	2.27	1.02	2.49
Desert Rock	ESA_LST_2P	-0.66	2.07	2.17	-3.85	0.39	3.87
	GT_ATS_2P	0.24	1.46	1.48	-1.79	0.40	1.83
Fort Peck	ESA_LST_2P	1.53	2.42	2.86	-0.45	1.57	1.63
	GT_ATS_2P	0.08	1.54	1.54	0.27	0.86	0.90
Goodwin Creek	ESA_LST_2P	0.79	1.54	1.73	2.00	0.82	2.16
	GT_ATS_2P	0.79	1.21	1.45	2.18	0.58	2.26
Penn State University	ESA_LST_2P	-0.27	1.38	1.41	1.01	1.30	1.65
	GT_ATS_2P	0.22	1.13	1.15	0.92	1.85	2.07
Sioux Falls	ESA_LST_2P	-0.44	0.90	1.00	-0.29	1.33	1.36
	GT_ATS_2P	-0.53	0.86	1.01	0.59	0.86	1.04
Table Mountain	ESA_LST_2P	1.53	2.58	3.00	-1.38	1.70	2.19
	GT_ATS_2P	1.55	2.46	2.91	-0.27	1.66	1.68
Southern Great Plains	ESA_LST_2P	-1.39	1.97	2.41	-1.50	1.41	2.06
	GT_ATS_2P	-1.09	1.08	1.53	-0.30	0.71	0.77

*Note.* Median ( $\mu$ ) differences, robust standard deviations ( $\sigma$ ), and root-mean-square errors (RMSEs) are presented for both day and night observations.

The validation (Table 5 and Figure 8) at the SURFRAD and ARM sites is in agreement with the findings at Gobabeb and Evora. GT\_ATS\_2P shows good agreement with the in situ LST with low mean difference and standard deviations. In general, the RMSEs are lower for GT\_ATS\_2P than for ESA\_LST\_2P. Figure 8 shows the results at selected stations, which represent different biomes. The line of best fit in most cases for GT\_ATS\_2P is close to the 1:1 line. The statistics show both mean differences and standard differences to generally be within 2 K. An exception being for Table Mountain, Colorado, which is sparsely vegetated. Here there is a tendency for GT\_LST\_2P to overestimate for high daytime temperatures and underestimate for low nighttime temperatures. This difference is in part captured by the increased uncertainty at higher temperatures but highlights a situation where the algorithm may not be operating optimally. Future evolution of the product will attempt to confront this. Overall, the mean absolute bias between in situ data and GT\_ATS\_2P is 1.00 K in the daytime and 1.08 K in the nighttime.

#### 4.2. Intercomparisons With a Reference LST Product

The validation against in situ LST is complemented with comparison between AATSR products (GT\_ATS\_2P and ESA\_LST\_2P) and a reference product derived from an alternative satellite instrument. While it is not possible to quantify the same metrics as for an in situ validation, an intercomparison can contribute important information with respect to spatial patterns in the parameter of interest. Here the AATSR LST are compared with SEVIRI LST generated by the European Organisation for the Exploitation of Meteorological Satellites (EUMETSAT) Satellite Applications Facility on Land Surface Analysis (LSA SAF product LSA-001) (Trigo et al., 2008, 2011).

The intercomparison here is carried out on a common 0.05° grid over the SEVIRI disk covering all of Africa plus southern and central Europe for all coincident observations during 2009, where temporal matchup is attained through linear interpolation of adjacent 15 min SEVIRI acquisitions to the AATSR acquisition time. Source data are cloud cleared prior to matchup, and only the highest-quality data are used. Monthly comparisons for day and night are composited from individual matchups. The bulk of the SEVIRI disk used here encompasses most ALB-2 biomes and is sufficiently covered by both instruments, which allows an identification of seasonal differences. Figure 9 details the differences for each AATSR product (GT\_ATS\_2P and ESA\_LST\_2P) with respect to the SEVIRI disk over Europe and Africa for each monthly composite separated by day and night. Spatial

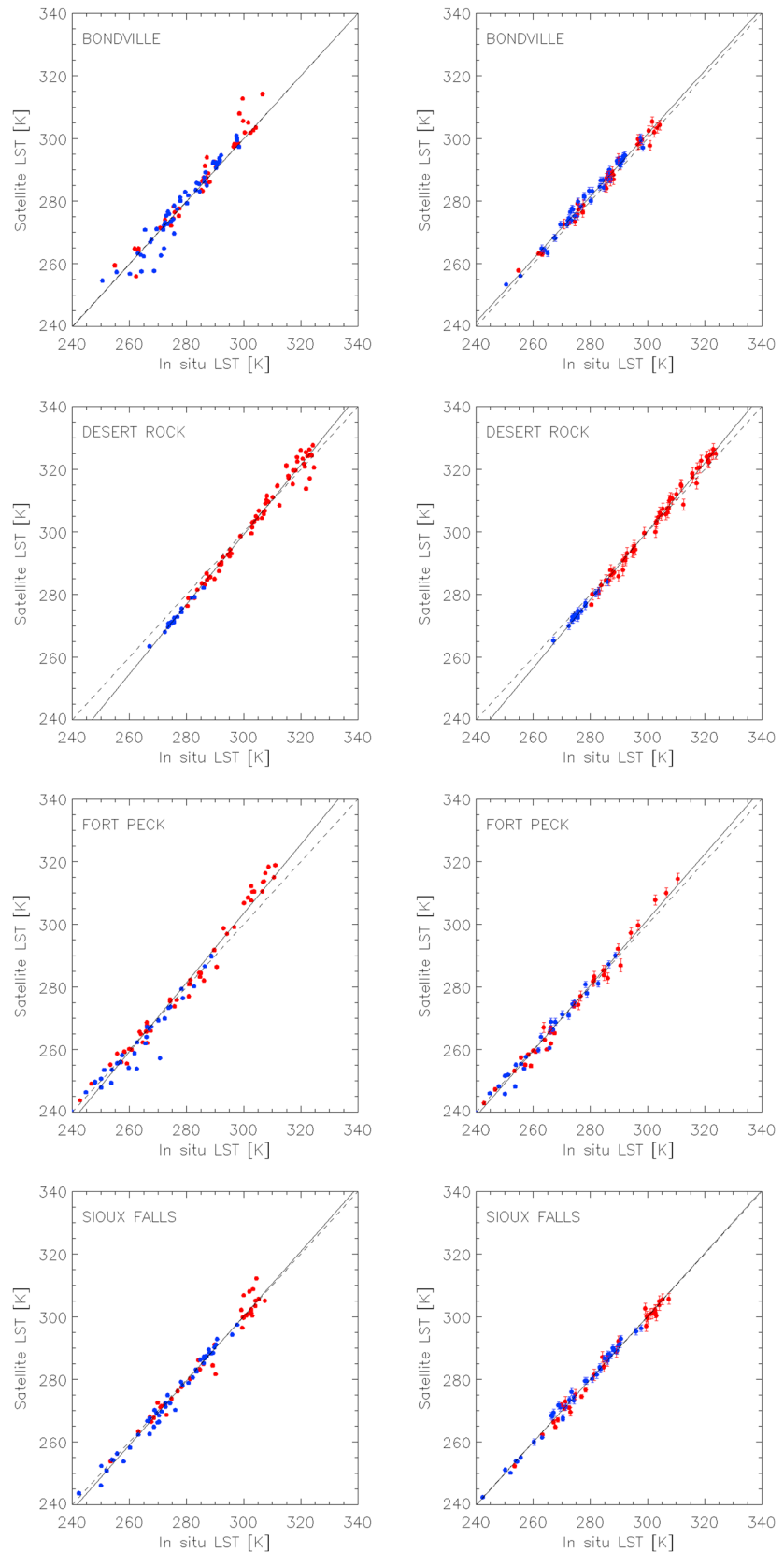


**Figure 8.** Scatterplots of GT\_ATS\_2P LST versus ground-based LST matchups for SURFRAD stations representing different biomes during 2009 for both day (red) and night (blue).

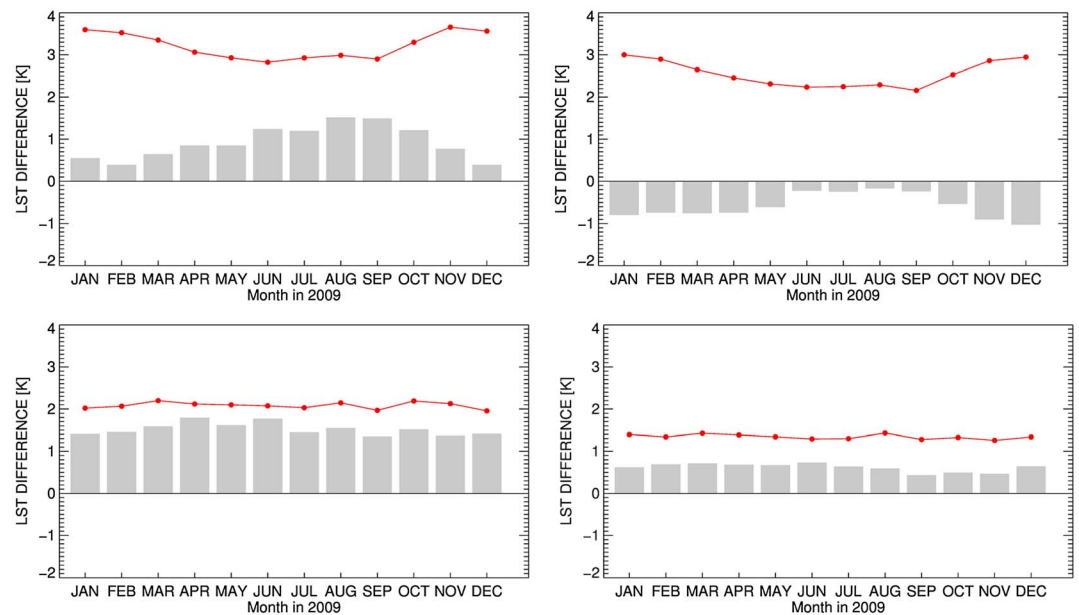


**Figure 9.** Monthly intercomparison composites during 2009 for both AATSR LST retrievals with respect to SEVIRI LST: (top row) ESA\_LST\_2P and (bottom row) GT\_ATS\_2P. (left column) Day composites and (right column) night composites. Median ( $\mu$ ) differences are presented as the bars, and robust standard deviations are presented as the points.

patterns for four selected months, representative of the seasonal variability, are also illustrated for day (Figure 10) and night (Figure 11).

In Figures 10 and 11 the GT\_ATS\_2P minus SEVIRI LST differences do not exhibit the unphysical LST gradients across geophysical regimes typically observed in ESA\_LST\_2P minus SEVIRI LST differences. This is due to replacing the  $0.5^\circ$  coarse resolution land cover and fractional vegetation auxiliary data in the ESA\_LST\_2P product with near 1 km resolution data in the GT\_ATS\_2P product. However, strong topographical features over the mountainous regions of southern and central Europe and the East African Rift (EAR) still affect the differences of both AATSR products with respect to SEVIRI. These observed differences, which are larger for daytime matchups, are negative over Europe and positive in the EAR. They can be attributed to SEVIRI observing proportionally more of the sunlit side of mountains for Europe than AATSR from its position in geostationary Earth orbit relative to the position of the Sun during the local morning overpass of AATSR, and less of the sunlit area of the EAR.

Both AATSR LST products exhibit an apparent cold bias during the European winter and warm bias during the European summer with respect to SEVIRI. The cold biases are larger for daytime observations, which is consistent with other intercomparison exercises (Noyes et al., 2006; Trigo et al., 2008). A probable cause of this apparent seasonality is the spatial anisotropy of LST from different viewing perspectives, which is stronger during the day when solar heating occurs. However, the amplitudes of the seasonal differences are smaller for GT\_ATS\_2P than for ESA\_LST\_2P.

A significant difference between GT\_ATS\_2P and ESA\_LST\_2P with respect to SEVIRI LST is over Africa. GT\_ATS\_2P is generally warmer than SEVIRI over much of the continent, particularly during the day. There is little evidence of a temperature dependency in this difference, since higher temperatures over the Sahara do not exhibit larger differences. The larger differences instead appear near the Eastern edge of the SEVIRI disk and are likely to be related to the respective viewing geometries of the different satellite sensors relative to the position of the Sun during the local morning overpass of AATSR. In contrast, the differences between ESA\_LST\_2P and SEVIRI over Africa are strongly negative over the Sahara and strongly positive over the Central African forests.

Figure 9 shows that while the overall monthly differences for ESA\_LST\_2P versus SEVIRI may be lower than for GT\_ATS\_2P the standard deviations are much larger. As Figures 10 and 11 show this is due to large positive and negative differences for ESA\_LST\_2P versus SEVIRI for different regions canceling each other out for the

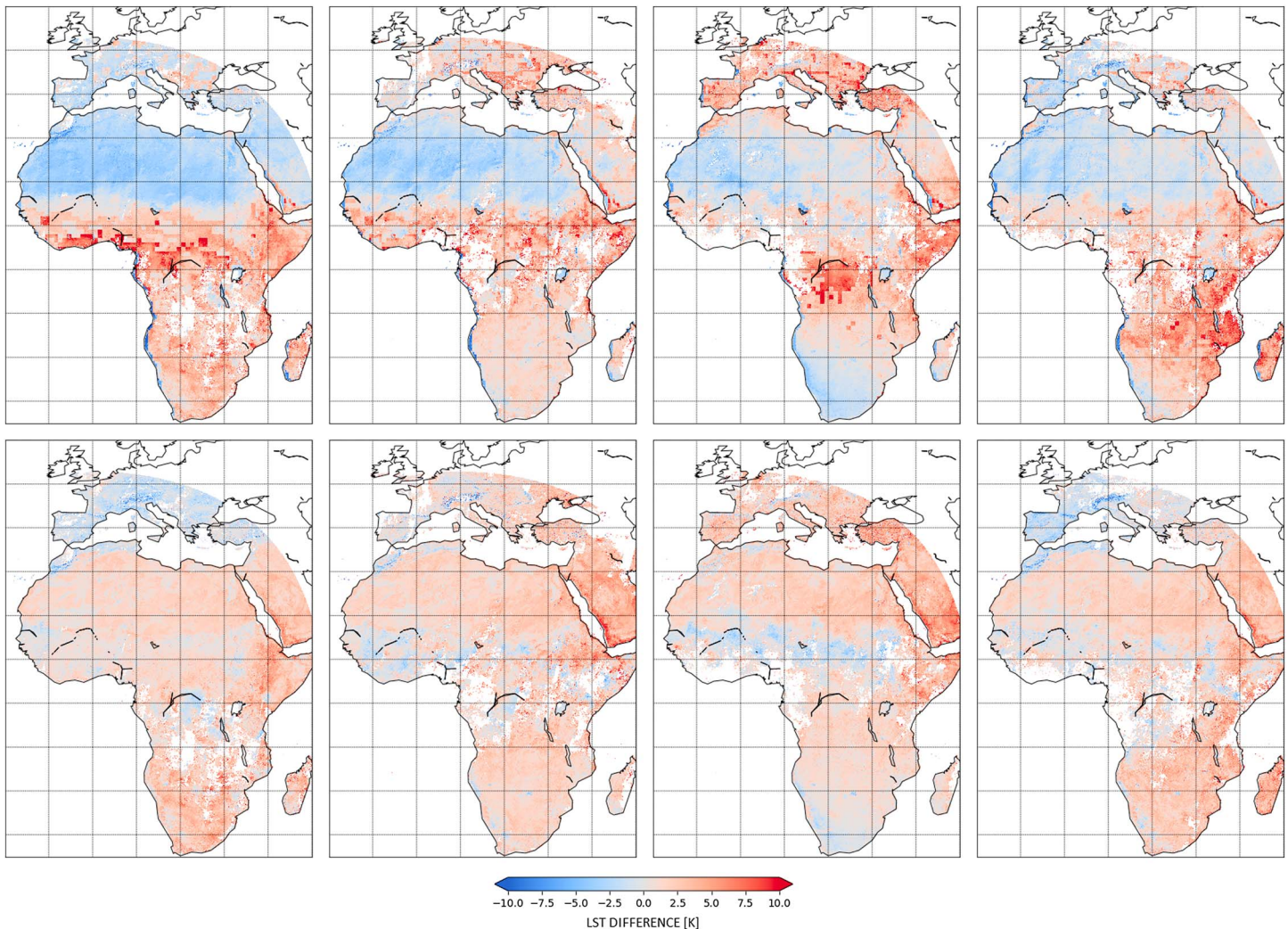


**Figure 10.** Monthly daytime composites for (first column) January, (second column) April, (third column) July, and (fourth column) October during 2009 (top row) for AATSR ESA\_LST\_2P minus SEVIRI LST and (bottom row) AATSR GT\_ATS\_2P minus SEVIRI LST.

most part. Remaining differences between GT\_ATS\_2P and SEVIRI are due to the respective retrieval algorithms, ancillary data, cloud clearing, and the spatiotemporal matchup process. Overall, GT\_ATS\_2P shows mean differences with SEVIRI, which are less than 1 K at night and 2 K during the day with standard deviations of less than 1.5 K and 2 K respectively.

## 5. Conclusions

In conclusion, we have shown that a split-window algorithm with nonexplicit emissivity but excellent statistical fitting can provide a globally robust retrieval algorithm with good precision. The LASPLAST has been used to generate 10 years of LST from AATSR for the first time with uncertainties.

Globally, robust retrieval coefficients have been generated to support the new auxiliary data used in LASPLAST with full traceability to the simulation input data. A uniform random sampling distribution selects input profiles that cover the full range of atmospheres and surfaces encountered, while also being representative of the mean conditions. The AATSR LST algorithm uses a single set of coefficients for the absolute nadir retrieval in which nonlinear water vapor and view angle sensitivity are parameterized. This across-track parameterization reduces the RMSEs for all biomes, both for both day and night, between LST retrieved from absolute nadir BT simulations and LST retrieved from edge-of-swath BT simulations.

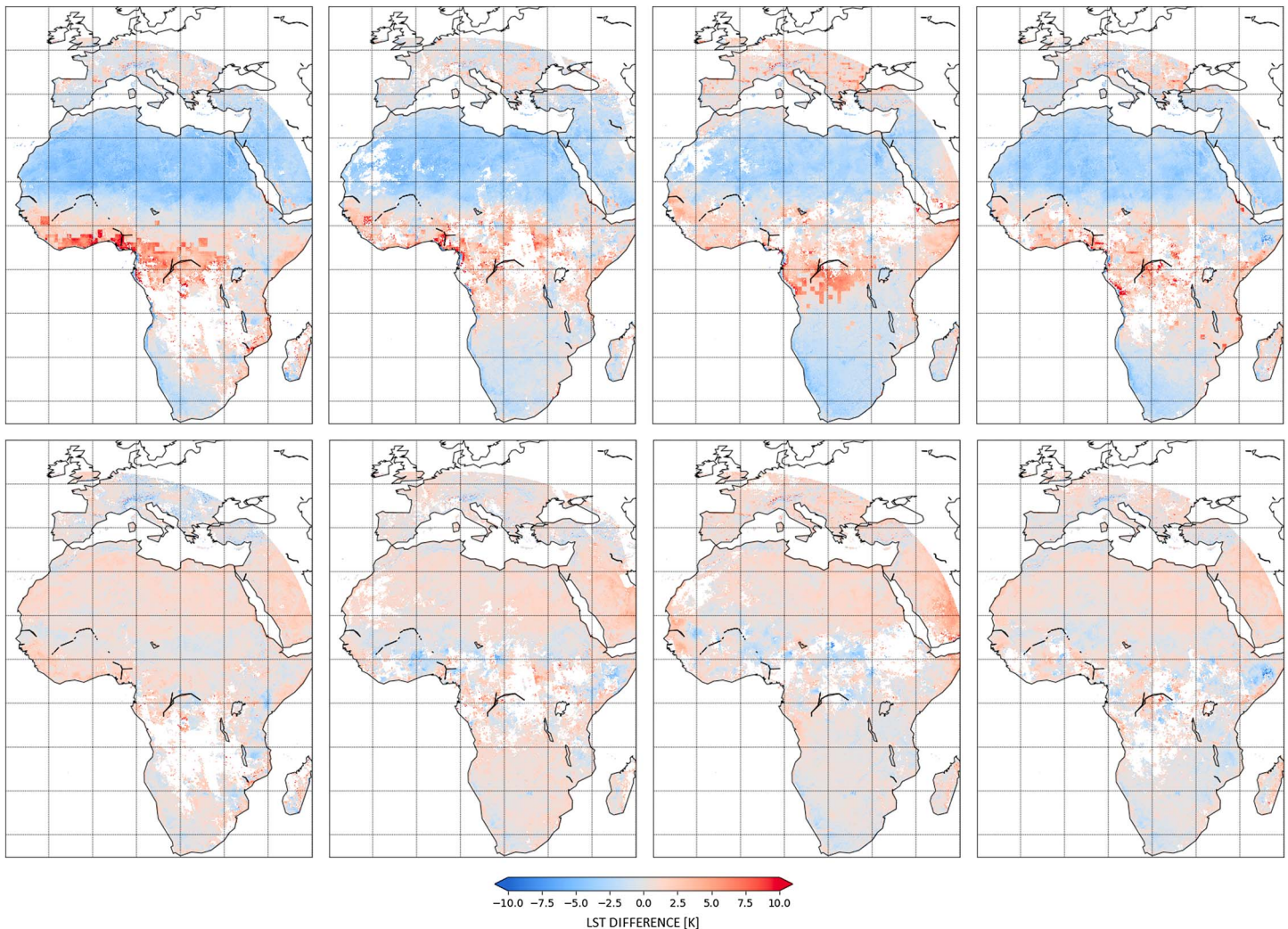


**Figure 11.** Monthly nighttime composites for (first column) January, (second column) April, (third column) July, and (fourth column) October during 2009 for (top row) AATSR ESA\_LST\_2P minus SEVIRI LST and (bottom row) AATSR GT\_ATS\_2P minus SEVIRI LST.

A further key improvement in LASPLAST is a probabilistic cloud mask based on concurrent simulations of clear-sky conditions. This is a thermal-only scheme making it equally robust for both day and night retrievals. It has been shown to perform better than the basic AATSR cloud masking available in the ESA\_LST\_2P product (Bulgin et al., 2014).

Information on the uncertainty of the LST data on a per pixel basis is a key refinement in LASPLAST. The uncertainty model is a three-component scheme, which represents the uncertainty from effects whose errors have distinct correlation properties. The random component is derived from the radiometric noise. The locally correlated component includes uncertainties from the fit to retrieval coefficients (combined atmospheric and absolute emissivity), variations in surface emissivity through vegetation change, and geolocation. The large-scale systematic component is estimated from uncertainty in the radiative transfer modeling and is very small.

The latest GlobTemperature LST product (GT\_ATS\_2P Version 1.0) has been produced through the LASPLAST framework. Validation of the GT\_ATS\_2P product with respect to in situ measurements acquired from the Gobabeb site in Namibia and the Evora site in Portugal during 2009 give average biases and standard deviations of  $-1.11$  K and  $1.14$  K, respectively, for Gobabeb and  $1.16$  K and  $1.40$  K, respectively, for Evora. These are lower than the equivalent statistics from the validation of the ESA\_LST\_2P product. Intercomparison over 1 year of the AATSR LST with respect to SEVIRI LST generated by LSA SAF shows the monthly differences

to be less for the GT\_ATS\_2P product than for ESA\_LST\_2P product for all months. Reductions in RMSEs are in the range of 0.24 to 1.76.

There are nevertheless some limitations with the LASPLAST retrieval scheme. First, that emissivity is dependent only on the combination of biome and fractional vegetation cover. In reality, this is not the case, as emissivity values can vary considerably over bare ground ( $f = 0$ ). This will result in greater differences between the maximum and minimum emissivity values at  $f = 0$  than at  $f = 1$ . For any given biome emissivity may not be invariant by latitude. For instance, ALB-2 class 15 (sparse vegetation) occurs in semideserts at low latitudes and midlatitudes but also at high latitudes in the transition zone between the Tundra and permanent ice, with different associations between emissivity and fractional vegetation. Future evolution of the algorithm could investigate latitudinal dependent coefficients per biome, and alternative approaches for channel emissivities for nonvegetated states. One approach for instance could be to utilize measurements recorded in the Advanced Spaceborne Thermal Emission and Reflection Radiometer spectral library, which provides a comprehensive source of over 2,400 laboratory measured spectra covering a wide variety of natural and artificial materials in the range of 0.4  $\mu\text{m}$  to 15.4  $\mu\text{m}$  (Baldrige et al., 2009).

Second, the effects of aerosol on the retrieval are not included. A number of studies for SST have indicated that retrievals in the presence of tropospheric mineral dust aerosol can be biased by several tenths of a degree (Good et al., 2012; Merchant et al., 2006). An equivalent impact is expected for LST retrievals. Future evolution will incorporate information on dust aerosol optical depth.

Third, validation over sea ice (not shown) suggests defining a distinct set of retrieval coefficients from those for the ice sheets and transient snow over land. The definition of a new biome to better represent the unique features of sea ice will be included in a future update of LASPLAST.

Finally, the algorithm does not take advantage of the dual-angle capability of AATSR. The advantages of a dual-angle retrieval for SST (Embury, Merchant, & Corlett., 2012) are though outweighed by disadvantages over land such as surface heterogeneity and nonsimultaneity of the two views (Prata, 2002). For homogeneous surfaces, Soria and Sobrino (2007) have illustrated that a dual-angle algorithm may retrieve LST with more accuracy in simulation but practice proved to be rather more difficult with considerably greater errors for dual-view methods compared to nadir-only. Further investigations would, however, be an advantage.

Despite these limitations, the results presented here clearly show GT\_ATS\_2P to be a valuable LST product. Validation shows the accuracy of the GT\_ATS\_2P product to be  $\sim 1$  K with respect to in situ observations and is supported by other recent work (Ouyang et al., 2017). This is in line with the target accuracy for LST in the most recent GCOS Implementation Plan (GCOS, 2016), indicating that the GT\_ATS\_2P product is suitable for integration into a climate data record for the ATSR series. This implementation of the LASPLAST retrieval formulation with the refinements described in this paper is being both for ATSR-2 data within GlobTemperature (GT\_AT2\_2P product) and also in an operational capacity within the Sentinel-3 Level-2 LST Instrument Processing Facility. This will, in time, lead to the ideal of a consistent retrieval from the ATSR series through to the SL\_2\_LST core product for SLSTR, which will support the Copernicus operational services and long-term records of LST.

Set within a global framework of LST instruments from low Earth and geostationary orbits, the ATSR-type instruments, including the SLSTR, will have a key role to play and with further work on radiometric calibration could play a reference standard role as they do for sea surface temperature. This is significant for future evolution of the satellite-based, global observing system for surface temperature both operationally and for climate data records. The merging of LST data sets requires a very good ability to cross-calibrate LST instruments radiometrically and inter-relate them at the LST data set level. The experience of uncertainty modeling within LASPLAST will be very helpful for the community in developing merged products, which should be of significant benefit to scientific community and to users of satellite data from a wide range of application sectors.

## References

- Anderson, M. C., Norman, J. M., Mecikalski, J. R., Otkin, J. A., & Kustas, W. P. (2007). A climatological study of evapotranspiration and moisture stress across the continental United States based on thermal remote sensing: 2. Surface moisture climatology. *Journal of Geophysical Research*, 112, D11112. <https://doi.org/10.1029/2006JD007507>
- Anderson, M. C., Kustas, W. P., Norman, J. M., Hain, C. R., Mecikalski, J. R., Schultz, L., ... Gao, F. (2011). Mapping daily evapotranspiration at field to continental scales using geostationary and polar orbiting satellite imagery. *Hydrology and Earth System Sciences*, 15, 223–239. <https://doi.org/10.5194/hess-15-223-2011>

## Acknowledgments

This work is jointly funded by the European Space Agency within the framework of the GlobTemperature project under the Data User Element of ESA's Fourth Earth Observation Envelope Programme (2013–2017) and a NERC grant to the National Centre for Earth Observation (NCEO) in the UK. This work utilizes AATSR data acquired from the Natural Environment Research Council Earth Observation Data Centre, profile data from the European Centre for Medium-range Weather Forecasts, land cover data from the Globcover Data User Element project, and fractional vegetation cover data from the European Commission funded Copernicus Global Land Service. SEVIRI LSTs were provided by the Land Surface Analysis Satellite Applications Facility (LSA SAF), a project funded by the European Organisation for the Exploitation of Meteorological Satellites (EUMETSAT), and in situ LST for the validation stations by Karlsruhe Institute of Technology (KIT). The authors would like to thank past and present colleagues at the University of Leicester, who have helped with the generation of plots and statistics: Olof Zeller, Tim Trent, and Michael Perry. Finally, we wish to express our gratitude to the reviewers of this paper. All data are freely accessible from the GlobTemperature Data Portal (<http://data.globtemperature.info/>).

- Arino, O., Gross, D., Ranera, F., Leroy, M., Bicheron, P., Brockman, C., ... Weber, J.-L. (2007). GlobCover: ESA service for global land cover from MERIS. In *IEEE International geoscience and remote sensing symposium* (pp. 2412–2415).
- Augustine, J. A., DeLuisi, J. J., & Long, C. N. (2000). SURFRAD—A national Surface Radiation Budget network for atmospheric research. *Bulletin of the American Meteorological Society*, 81(10), 2341–2357. [https://doi.org/10.1175/1520-0477\(2000\)081%3C2341:SANSRB%3E2.3.CO;2](https://doi.org/10.1175/1520-0477(2000)081%3C2341:SANSRB%3E2.3.CO;2)
- Baldrige, A. M., Hook, S. J., Grove, C. I., & Rivera, G. (2009). The ASTER spectral library version 2.0. *Remote Sensing of Environment*, 113, 711–715. <https://doi.org/10.1016/j.rse.2008.11.007>
- Baret, F., Weiss, M., Lacaze, R., Camacho, F., Makhmara, H., Pacholczyk, P., & Smets, B. (2013). GEOV1: LAI and FAPAR essential climate variables and FCOVER global time series capitalizing over existing products. Part 1: Principles of development and production. *Remote Sensing of Environment*, 137, 299–309. <https://doi.org/10.1016/j.rse.2012.12.027>
- Bauduin, S., Clarisse, L., Theunissen, M., George, M., Hurtmans, D., Clerbaux, C., & Coheur, P.-F. (2017). IASI's sensitivity to near-surface carbon monoxide (CO): Theoretical analyses and retrievals on test cases. *Journal of Quantitative Spectroscopy and Radiative Transfer*, 189, 428–440. <https://doi.org/10.1016/j.jqsrt.2016.12.022>
- Becker, F., & Li, Z. L. (1990). Towards a local split window method over land surfaces. *International Journal of Remote Sensing*, 11(3), 369–393. <https://doi.org/10.1080/01431169008955028>
- Birks, A. R. (2007). Improvements to the AATSR IPF relating to land surface temperature retrieval and cloud clearing over land laboratory. *AATSR Technical Note*. Oxfordshire: Rutherford Appleton.
- Birks, A. R. (2010). Instrument pixel co-ordinates and measurement times from AATSR products (AATSR expert support laboratory technical note).
- Bosilovich, M. G., Radakovich, J. D., da Silva, A., Todling, R., & Verter, F. (2007). Skin temperature analysis and bias correction in a coupled land-atmosphere data assimilation system. *Journal of the Meteorological Society of Japan*, 85A, 205–228. <https://doi.org/10.2151/jmsj.85A.205>
- Bulgin, C. E., Sembhi, H., Ghent, D., Remedios, J., & Merchant, C. J. (2014). Cloud clearing techniques over land for land surface temperature retrieval from the Advanced Along Track Scanning Radiometer. *International Journal of Remote Sensing*, 35(10), 3594–3615. <https://doi.org/10.1080/01431161.2014.907941>
- Bulgin, C. E., Embury, O., Corlett, G., & Merchant, C. J. (2016). Independent uncertainty estimates for coefficient based sea surface temperature retrieval from the Along-Track Scanning Radiometer instruments. *Remote Sensing of Environment*, 178, 213–222. Retrieved from <http://www.sciencedirect.com/science/article/pii/S0034425716300505>, <https://doi.org/10.1016/j.rse.2016.02.022>
- Camacho, F., Cernicharo, J., Lacaze, R., Baret, F., & Weiss, M. (2013). GEOV1: LAI, FAPAR essential climate variables and FCOVER global time series capitalizing over existing products. Part 2: Validation and intercomparison with reference products. *Remote Sensing of Environment*, 137, 310–329. <https://doi.org/10.1016/j.rse.2013.02.030>
- Clough, S. A., Shephard, M. W., Mlawer, E., Delamere, J. S., Iacono, M., Cady-Pereira, K., ... Brown, P. D. (2005). Atmospheric radiative transfer modeling: A summary of the AER codes. *Journal of Quantitative Spectroscopy & Radiative Transfer*, 91, 233–244. <https://doi.org/10.1016/j.jqsrt.2004.05.058>
- Coll, C., & Caselles, V. (1997). A split-window algorithm for land surface temperature from advanced very high resolution radiometer data: Validation and algorithm comparison. *Journal of Geophysical Research*, 102(D14), 16,697–16,713. <https://doi.org/10.1029/97JD00929>
- Coll, C., Caselles, V., Galve, J. M., Valor, E., Niclos, R., Sanchez, J. M., & Rivas, R. (2005). Ground measurements for the validation of land surface temperatures derived from AATSR and MODIS data. *Remote Sensing of Environment*, 97, 288–300. <https://doi.org/10.1016/j.rse.2005.05.007>
- Coll, C., Caselles, V., Galve, J. M., Valor, E., Niclòs, R., & Sánchez, J. M. (2006). Evaluation of split-window and dual-angle correction methods for land surface temperature retrieval from Envisat/Advanced Along Track Scanning Radiometer (AATSR) data. *Journal of Geophysical Research*, 111, D12105. <https://doi.org/10.1029/2005JD006830>
- Coll, C., Valor, E., Galve, J. M., Mira, M., Bisquert, M., Garcia-Santos, V., ... Caselles, V. (2012). Long-term accuracy assessment of land surface temperatures derived from the Advanced Along-Track Scanning Radiometer. *Remote Sensing of Environment*, 116, 211–225. <https://doi.org/10.1016/j.rse.2010.01.027>
- Cuenca, J., & Sobrino, J. A. (2004). Experimental measurements for studying angular and spectral variation of thermal infrared emissivity. *Applied Optics*, 43, 4598–4602. <https://doi.org/10.1364/AO.43.004598>
- Dee, D. P., Uppala, S. M., Simmons, A. J., Berrisford, P., Poli, P., Kobayashi, S., ... Vitart, F. (2011). The ERA-Interim reanalysis: Configuration and performance of the data assimilation system. *Quarterly Journal of the Royal Meteorological Society*, 137(656), 553–597. <https://doi.org/10.1002/qj.828>
- Donlon, C. J., Martina, M., Starka, J., Roberts-Jones, J., Fiedler, E., & Wimmer, W. (2012). The Operational Sea Surface Temperature and Sea Ice Analysis (OSTIA) system. *Remote Sensing of Environment*, 116, 140–158. <https://doi.org/10.1016/j.rse.2010.10.017>
- Dorman, J. L., & Sellers, P. J. (1989). A global climatology of albedo, roughness length and stomatal-resistance for atmospheric general-circulation models as represented by the Simple Biosphere model (SiB). *Journal of Applied Meteorology*, 28(9), 833–855. [https://doi.org/10.1175/1520-0450\(1989\)028%3C0833:AGCOAR%3E2.0.CO;2](https://doi.org/10.1175/1520-0450(1989)028%3C0833:AGCOAR%3E2.0.CO;2)
- Eastwood, S., & Andersen, S. (2007). Masking of sea ice for METOP SST retrieval (Danish Meteorological Institute report).
- Embury, O., Merchant, C. J., & Corlett, G. K. (2012). A reprocessing for climate of sea surface temperature from the along-track scanning radiometers: Initial validation, accounting for skin and diurnal variability effects. *Remote Sensing of Environment*, 116, 62–78. <https://doi.org/10.1016/j.rse.2011.02.028>
- Embury, O., Merchant, C. J., & Filipiak, M. J. (2012). A reprocessing for climate of sea surface temperature from the along-track scanning radiometers: Basis in radiative transfer. *Remote Sensing of Environment*, 116, 32–46. <https://doi.org/10.1016/j.rse.2010.10.016>
- Ermida, S., Trigo, I., DaCamara, C., Göttsche, F., Olesen, F., & Hulley, G. (2014). Validation of remotely sensed surface temperature over an oak woodland landscape—The problem of viewing and illumination geometries. *Remote Sensing of Environment*, 148, 16–27. <https://doi.org/10.1016/j.rse.2014.03.016>
- Ermida, S. L., DaCamara, C. C., Trigo, I. F., Pires, A. C., Ghent, D., & Remedios, J. (2017). Modelling directional effects on remotely sensed land surface temperature. *Remote Sensing of Environment*, 190, 56–69. <https://doi.org/10.1016/j.rse.2016.12.008>
- Freitas, S. C., Trigo, I. F., Bioucas-Dias, J. M., & Gottsche, F. M. (2010). Quantifying the uncertainty of land surface temperature retrievals from SEVIRI/Meteosat. *IEEE Transactions on Geoscience and Remote Sensing*, 48, 523–534. <https://doi.org/10.1109/TGRS.2009.2027697>
- GCOS (2016). The global observing system for climate: Implementation needs (GCOS-200).
- Ghent, D., Kaduk, J., Remedios, J., Ardo, J., & Balzter, H. (2010). Assimilation of land surface temperature into the land surface model JULES with an ensemble Kalman filter. *Journal of Geophysical Research*, 115, D19112. <https://doi.org/10.1029/2010JD014392>
- Ghent, D., Kaduk, J., Remedios, J., & Balzter, H. (2011). Data assimilation into land surface models: The implications for climate feedbacks. *International Journal of Remote Sensing*, 32, 617–632. <https://doi.org/10.1080/01431161.2010.517794>

- Gillespie, A., Rokugawa, S., Matsunaga, T., Cothren, J. S., Hook, S., & Kahle, A. B. (1998). A temperature and emissivity separation algorithm for Advanced Spaceborne Thermal Emission and Reflection Radiometer (ASTER) images. *IEEE Transactions on Geoscience and Remote Sensing*, 36(4), 1113–1126. <https://doi.org/10.1109/36.700995>
- Gleason, A. C. R., Prince, S. D., Goetz, S. J., & Small, J. (2002). Effects of orbital drift on land surface temperature measured by AVHRR thermal sensors. *Remote Sensing of Environment*, 79(2-3), 147–165. [https://doi.org/10.1016/S0034-4257\(01\)00269-3](https://doi.org/10.1016/S0034-4257(01)00269-3)
- Good, E. J., Kong, X., Embury, O., Merchant, C. J., & Remedios, J. J. (2012). An infrared desert dust index for the Along-Track Scanning Radiometers. *Remote Sensing of Environment*, 116, 159–176. <https://doi.org/10.1016/j.rse.2010.06.016>
- Gottsche, F. M., & Hulley, G. C. (2012). Validation of six satellite-retrieved land surface emissivity products over two land cover types in a hyper-arid region. *Remote Sensing of Environment*, 124, 149–158. <https://doi.org/10.1016/j.rse.2012.05.010>
- Gottsche, F. M., Olesen, F. S., & Bork-Unkelbach, A. (2013). Validation of land surface temperature derived from MSG/SEVIRI with in situ measurements at Gobabeb, Namibia. *International Journal of Remote Sensing*, 34(9-10), 3069–3083. <https://doi.org/10.1080/01431161.2012.716539>
- Götsche, F. M., Olesen, F., Trigo, I., Bork-Unkelbach, A., & Martin, M. (2016). Long term validation of land surface temperature retrieved from MSG/SEVIRI with continuous in-situ measurements in Africa. *Remote Sensing*, 8(5), 410. <https://doi.org/10.3390/rs8050410>
- Hocking, J., Rayer, P., Saunders, R., Matricardi, M., Geer, A., & Brunel, P. (2011). RTTOV v10 users guide. EUMETSAT satellite application facility on numerical weather prediction. NWSAF-MO-UD-023. Version 1.5.
- Huang, C. L., Li, X., & Lu, L. (2008). Retrieving soil temperature profile by assimilating MODIS LST products with ensemble Kalman filter. *Remote Sensing of Environment*, 112, 1320–1336. <https://doi.org/10.1016/j.rse.2007.03.028>
- Hulley, G. C., & Hook, S. J. (2011). Generating consistent land surface temperature and emissivity products between ASTER and MODIS data for Earth science research. *IEEE Transactions on Geoscience and Remote Sensing*, 49, 1304–1315. <https://doi.org/10.1109/TGRS.2010.2063034>
- Hulley, G. C., Hook, S. J., Manning, E., Lee, S. Y., & Fetzer, E. (2009). Validation of the Atmospheric Infrared Sounder (AIRS) version 5 land surface emissivity product over the Namib and Kalahari deserts. *Journal of Geophysical Research*, 114, D19104. <https://doi.org/10.1029/2009JD012351>
- Hulley, G. C., Hughes, C. G., & Hook, S. J. (2012). Quantifying uncertainties in land surface temperature and emissivity retrievals from ASTER and MODIS thermal infrared data. *Journal of Geophysical Research*, 117, D23113. <https://doi.org/10.1029/2012JD018506>
- Istomina, L. G., von Hoyningen-Huene, W., Kokhanovsky, A. A., & Burrows, J. P. (2010). The detection of cloud-free snow-covered areas using AATSR measurements. *Atmospheric Measurement Techniques*, 3, 1005–1017. <https://doi.org/10.5194/amt-3-1005-2010>
- Jimenez-Munoz, J. C., & Sobrino, J. A. (2008). Split-window coefficients for land surface temperature retrieval from low-resolution thermal infrared sensors. *IEEE Geoscience and Remote Sensing Letters*, 5, 806–809. <https://doi.org/10.1109/LGRS.2008.2001636>
- Jin, M. L., Dickinson, R. E., & Vogelmann, A. M. (1997). A comparison of CCM2-BATS skin temperature and surface-air temperature with satellite and surface observations. *Journal of Climate*, 10(7), 1505–1524. [https://doi.org/10.1175/1520-0442\(1997\)010%3C1505:ACOCBS%3E2.0.CO;2](https://doi.org/10.1175/1520-0442(1997)010%3C1505:ACOCBS%3E2.0.CO;2)
- Kabsch, E., Olesen, F., & Prata, F. (2008). Initial results of the land surface temperature (LST) validation with the Evora, Portugal ground-truth station measurements. *International Journal of Remote Sensing*, 29, 5329–5345. <https://doi.org/10.1080/01431160802036326>
- Koenig, M., & de Coning, E. (2009). The MSG global instability indices product and its use as a nowcasting tool. *Weather and Forecasting*, 24, 272–285. <https://doi.org/10.1175/2008WAF2222141.1>
- Li, Z.-L., & Becker, F. (1993). Feasibility of land surface temperature and emissivity determination from AVHRR data. *Remote Sensing of Environment*, 43(1), 67–85. [https://doi.org/10.1016/0034-4257\(93\)90065-6](https://doi.org/10.1016/0034-4257(93)90065-6)
- Li, Z.-L., Tang, B.-H., Wu, H., Ren, H., Yan, G., Wan, Z., ... Sobrino, J. A. (2013). Satellite-derived land surface temperature: Current status and perspectives. *Remote Sensing of Environment*, 131, 14–37. <https://doi.org/10.1016/j.rse.2012.12.008>
- Li, S., Yu, Y., Sun, D., Tarpley, D., Zhan, X., & Chiu, L. (2014). Evaluation of 10 year AQUA/MODIS land surface temperature with SURFRAD observations. *International Journal of Remote Sensing*, 35(3), 830–856. <https://doi.org/10.1080/01431161.2013.873149>
- Liu, Y., Yu, Y., Yu, P., Götsche, F., & Trigo, I. (2015). Quality assessment of S-NPP VIIRS land surface temperature product. *Remote Sensing*, 7(9), 12,215–12,241. <https://doi.org/10.3390/rs70912215>
- Llewellyn-Jones, D., & Remedios, J. (2012). The Advanced Along Track Scanning Radiometer (AATSR) and its predecessors ATSR-1 and ATSR-2: An introduction to the special issue. *Remote Sensing of Environment*, 116, 1–3. <https://doi.org/10.1016/j.rse.2011.06.002>
- Llewellyn-Jones, D., Edwards, M. C., Mutlow, C. T., Birks, A. R., Barton, I. J., & Tait, H. (2001). AATSR: Global-change and surface-temperature measurements from Envisat. *Esa Bulletin-European Space Agency*, 11–21.
- McMillin, L. M. (1975). Estimation of sea surface temperatures from two infrared window measurements with different absorption. *Journal of Geophysical Research*, 80(36), 5113–5117. <https://doi.org/10.1029/JC080i036p05113>
- Merchant, C. J., & Le Borgne, P. (2004). Retrieval of sea surface temperature from space, based on modeling of infrared radiative transfer: Capabilities and limitations. *Journal of Atmospheric and Oceanic Technology*, 21, 1734–1746. <https://doi.org/10.1175/JTECH1667.1>
- Merchant, C. J., Harris, A. R., Murray, M. J., & Zavody, A. M. (1999). Toward the elimination of bias in satellite retrievals of sea surface temperature 1. Theory, modeling and interalgorithm comparison. *Journal of Geophysical Research*, 104(C10), 23,565–23,578. <https://doi.org/10.1029/1999JC900105>
- Merchant, C. J., Embury, O., Le Borgne, P., & Bellec, B. (2006). Saharan dust in nighttime thermal imagery: Detection and reduction of related biases in retrieved sea surface temperature. *Remote Sensing of Environment*, 104, 15–30. <https://doi.org/10.1016/j.rse.2006.03.007>
- Merchant, C. J., Embury, O., Rayner, N. A., Berry, D. I., Corlett, G. K., Lean, K., ... Saunders, R. (2012). A 20 year independent record of sea surface temperature for climate from Along-Track Scanning Radiometers. *Journal of Geophysical Research*, 117, C12013. <https://doi.org/10.1029/2012JC008400>
- Merchant, C. J., Matthiesen, S., Rayner, N. A., Remedios, J. J., Jones, P. D., Olesen, F., ... Hulley, G. C. (2013). The surface temperatures of Earth: Steps towards integrated understanding of variability and change. *Geosciences Instruments & Methods Data Systems*, 2(2), 305–321. <https://doi.org/10.5194/gi-2-305-2013>
- Moran, M. S. (2003). Thermal infrared measurement as an indicator of plant ecosystem health. In D. A. Quattrochi & J. Luval (Eds.), *Thermal Remote Sensing in Land Surface Processes* (Chap. 8, pp. 257–282). Boca Raton, FL: CRC Press, Taylor and Francis.
- Morris, V. R. (2006). Infrared thermometer (IRT) handbook (ARM TR-015). Atmospheric Radiation Measurement, Climate Research Facility, U. S. Department of Energy. Retrieved from [https://www.arm.gov/publications/tech\\_reports/handbooks/irt\\_handbook.pdf](https://www.arm.gov/publications/tech_reports/handbooks/irt_handbook.pdf)
- Nightingale, T. J., & Birks, A. R. (2004). AATSR algorithm verification: Comparison of AATSR and ATSR-2 data (AATSR technical note).
- Norman, J. M., & Becker, F. (1995). Terminology in thermal infrared remote sensing of natural surfaces. *Agricultural and Forest Meteorology*, 77(3-4), 153–166. [https://doi.org/10.1016/0168-1923\(95\)02259-Z](https://doi.org/10.1016/0168-1923(95)02259-Z)

- Noyes, E. J. (2006). Technical assistance for the validation of AATSR land surface temperature products, final report—February 2006 (report to European Space Agency).
- Noyes, E. J. (2007). Technical assistance for the validation of AATSR land surface temperature products, contract extension final report—January 2007 (report to European Space Agency).
- Noyes, E. J., Good, S., Corlett, G., Kong, X., Remedios, J., & Llewellyn-Jones, D. (2006). AATSR LST product validation. In *Second working meeting on MERIS and AATSR calibration and geophysical validation (MAVT-2006)*. Frascati, Italy: ESRIN.
- Noyes, E. J., Corlett, G., Remedios, J., Kong, X., & Llewellyn-Jones, D. (2007). An accuracy assessment of AATSR LST data using empirical and theoretical methods. In *Envisat Symposium 2007, ESA SP-636*. Montreux, Switzerland.
- Noyes, E. J., Soria, G., Sobrino, J. A., Remedios, J. J., Llewellyn-Jones, D. T., & Corlett, G. K. (2007). AATSR land surface temperature product algorithm verification over a WATERMED site. *Advances in Space Research*, 39, 171–178. <https://doi.org/10.1016/j.asr.2006.02.024>
- O'Hara, S. (2013). AATSR 12 micron anomaly review board—Final report (report to European Space Agency - IDEAS-VEG-OQC-REP-1274).
- Oltra-Carrio, R., Sobrino, J. A., Franch, B., & Nerry, F. (2012). Land surface emissivity retrieval from airborne sensor over urban areas. *Remote Sensing of Environment*, 123, 298–305. <https://doi.org/10.1016/j.rse.2012.03.007>
- Ouyang, X., Chen, D., Duan, S.-B., Lei, Y., Dou, Y., & Hu, G. (2017). Validation and analysis of long-term AATSR land surface temperature product in the Heihe River basin, China. *Remote Sensing*, 9(2), 152. <https://doi.org/10.3390/rs9020152>
- Peres, L. F., & DaCamara, C. C. (2005). Emissivity maps to retrieve land-surface temperature from MSG/SEVIRI. *IEEE Transactions on Geoscience and Remote Sensing*, 43, 1834–1844. <https://doi.org/10.1109/TGRS.2005.851172>
- Pinheiro, A. C. T., Privette, J. L., & Guillevic, P. (2006). Modeling the observed angular anisotropy of land surface temperature in a savanna. *IEEE Transactions on Geoscience and Remote Sensing*, 44, 1036–1047. <https://doi.org/10.1109/TGRS.2005.863827>
- Prata, A. J. (1993). Land-surface temperatures derived from the advanced very high-resolution radiometer and the Along-Track Scanning Radiometer. 1. Theory. *Journal of Geophysical Research*, 98(D9), 16,689–16,702. <https://doi.org/10.1029/93JD01206>
- Prata, A. J. (1994). Land-surface temperatures derived from the advanced very high-resolution radiometer and the Along-Track Scanning Radiometer. 2. Experimental results and validation of AVHRR algorithms. *Journal of Geophysical Research*, 99(D6), 13,025–13,058. <https://doi.org/10.1029/94JD00409>
- Prata, F. (2002). Land surface temperature measurement from space: AATSR algorithm theoretical basis document.
- Prata, F. (2011). Water vapour sensitivity of the (A)ATSR LST algorithm (report to European Space Agency).
- Privette, J. L., Fowler, C., Wick, G. A., Baldwin, D., & Emery, W. J. (1995). Effects of orbital drift on advanced very high resolution radiometer products: Normalized difference vegetation index and sea surface temperature. *Remote Sensing of Environment*, 53(3), 164–171. [https://doi.org/10.1016/0034-4257\(95\)00083-D](https://doi.org/10.1016/0034-4257(95)00083-D)
- Ramsey, B. H. (1998). The interactive multisensor snow and ice mapping system. *Hydrological Processes*, 12(10-11), 1537–1546. [https://doi.org/10.1002/\(SICI\)1099-1085\(199808/09\)12:10<11%3C1537::AID-HYP679%3E3.0.CO;2-A](https://doi.org/10.1002/(SICI)1099-1085(199808/09)12:10<11%3C1537::AID-HYP679%3E3.0.CO;2-A)
- Randel, D. L., VonderHaar, T. H., Ringerud, M. A., Stephens, G. L., Greenwald, T. J., & Combs, C. L. (1996). A new global water vapor dataset. *Bulletin of the American Meteorological Society*, 77(6), 1233–1246. [https://doi.org/10.1175/1520-0477\(1996\)077%3C1233:ANGWVD%3E2.0.CO;2](https://doi.org/10.1175/1520-0477(1996)077%3C1233:ANGWVD%3E2.0.CO;2)
- Rhoads, J., Dubayah, R., Lettenmaier, D., O'Donnell, G., & Lakshmi, V. (2001). Validation of land surface models using satellite-derived surface temperature. *Journal of Geophysical Research*, 106(D17), 20,085–20,099. <https://doi.org/10.1029/2001JD900196>
- Rossow, W. B., & Schiffer, R. A. (1999). Advances in understanding clouds from ISCCP. *Bulletin of the American Meteorological Society*, 71, 2–20.
- Saunders, R. W. (1986). An Automated Scheme for the Removal of Cloud Contamination from AVHRR Radiances over Western Europe. *International Journal of Remote Sensing*, 7, 867–886. <https://doi.org/10.1080/01431168608948896>
- Saunders, R., Hocking, J., Rayer, P., Matricardi, M., Geer, A., Bormann, N., ... Aires, F. (2012). RTTOV-10 science and validation report.
- Seemann, S. W., Borbas, E. E., Knuteson, R. O., Stephenson, G. R., & Huang, H. L. (2008). Development of a global infrared land surface emissivity database for application to clear sky sounding retrievals from multispectral satellite radiance measurements. *Journal of Applied Meteorology and Climatology*, 47, 108–123. <https://doi.org/10.1175/2007JAMC1590.1>
- Smith, D. (1999). AATSR infra-red radiometric calibration report.
- Smith, D. (2012). ENVISAT AATSR instrument performance—End of mission report. *AATSR Technical Note (Ref: PO-RP-RAL-AT-0621)*.
- Smith, D. (2014). Empirical nonlinearity correction for 12  $\mu\text{m}$  channel. *AATSR Technical Note (Ref: PO-TN-RAL-AT-0562)*.
- Sobrino, J. A., Jimenez-Munoz, J. C., Soria, G., Romaguera, M., Guanter, L., Moreno, J., ... Martincz, P. (2008). Land surface emissivity retrieval from different VNIR and TIR sensors. *IEEE Transactions on Geoscience and Remote Sensing*, 46, 316–327. <https://doi.org/10.1109/TGRS.2007.904834>
- Sobrino, J. A., Jiménez-Muñoz, J. C., Soria, G., Ruescas, A. B., Danne, O., Brockmann, C., ... Göttsche, F. M. (2016). Synergistic use of MERIS and AATSR as a proxy for estimating land surface temperature from Sentinel-3 data. *Remote Sensing of Environment*, 179, 149–161. <https://doi.org/10.1016/j.rse.2016.03.035>
- Soil Survey Staff (1999). Soil taxonomy: A basic system of soil classification for making and interpreting soil surveys. In *Natural resources conservation service. U.S. Department of Agriculture Handbook 436*.
- Soria, G., & Sobrino, J. A. (2007). ENVISAT/AATSR derived land surface temperature over a heterogeneous region. *Remote Sensing of Environment*, 111, 409–422. <https://doi.org/10.1016/j.rse.2007.03.017>
- Steinke, S., Eikenberg, S., Löhnert, U., Dick, G., Klocke, D., Di Girolamo, P., & Crewell, S. (2015). Assessment of small-scale integrated water vapour variability during HOPE. *Atmospheric Chemistry and Physics*, 15(5), 2675–2692. <https://doi.org/10.5194/acp-15-2675-2015>
- Trigo, I. F., Monteiro, I. T., Olesen, F., & Kabsch, E. (2008). An assessment of remotely sensed land surface temperature. *Journal of Geophysical Research*, 113, D17108. <https://doi.org/10.1029/2008JD010035>
- Trigo, I. F., DaCamara, C. C., Viterbo, P., Roujean, J.-L., Olesen, F., Barroso, C., ... Arboleda, A. (2011). The satellite application facility on land surface analysis. *International Journal of Remote Sensing*, 32(10), 2725–2744. <https://doi.org/10.1080/01431161003743199>
- Veal, K. L., Corlett, G. K., Ghent, D., Llewellyn-Jones, D. T., & Remedios, J. J. (2013). A time series of mean global skin-SST anomaly using data from ATSR-2 and AATSR. *Remote Sensing of Environment*, 135, 64–76. <https://doi.org/10.1016/j.rse.2013.03.028>
- Verger, A., Baret, F., & Camacho, F. (2011). Optimal modalities for radiative transfer-neural network estimation of canopy biophysical characteristics: Evaluation over an agricultural area with CHRIS/PROBA observations. *Remote Sensing of Environment*, 115(2), 415–426. <https://doi.org/10.1016/j.rse.2010.09.012>
- Vinnikov, K. Y., Yu, Y., Goldberg, M. D., Tarpley, D., Romanov, P., Laszlo, I., & Chen, M. (2012). Angular anisotropy of satellite observations of land surface temperature. *Geophysical Research Letters*, 39, L23802. <https://doi.org/10.1029/2012GL054059>
- Vogelmann, H., Sussmann, R., Trickl, T., & Reichert, A. (2015). Spatiotemporal variability of water vapor investigated using lidar and FTIR vertical soundings above the Zugspitze. *Atmospheric Chemistry and Physics*, 15(6), 3135–3148. <https://doi.org/10.5194/acp-15-3135-2015>

- Wan, Z. (2008). New refinements and validation of the MODIS land surface temperature/emissivity products. *Remote Sensing of Environment*, 112(1), 59–74. <https://doi.org/10.1016/j.rse.2006.06.026>
- Wan, Z., & Dozier, J. (1996). A generalized split-window algorithm for retrieving land surface temperature from space. *IEEE Transactions on Geoscience and Remote Sensing*, 34, 892–905.
- Wan, Z., & Hulley, G. (2015). MOD11C1 MODIS/Terra land surface temperature/emissivity daily L3 global 0.05Deg CMG V006. NASA EOSDIS land processes DAAC. <https://doi.org/10.5067/MODIS/MOD11C1.006>
- Yu, Y., Tarpley, D., Privette, J. L., Flynn, L. E., Xu, H., Chen, M., ... Tian, Y. (2012). Validation of GOES-R satellite land surface temperature algorithm using SURFRAD ground measurements and statistical estimates of error properties. *IEEE Transactions on Geoscience and Remote Sensing*, 50, 704–713. <https://doi.org/10.1109/TGRS.2011.2162338>
- Zavody, A. M., Mutlow, C. T., & Llewellynjones, D. T. (1995). A radiative-transfer model for sea-surface temperature retrieval for the Along-Track Scanning Radiometer. *Journal of Geophysical Research*, 100(C1), 937–952. <https://doi.org/10.1029/94JC02170>
- Zeller, O., & Ghent, D. (2011). ATSR absolute geolocation accuracy: Observed shift between AATSR brightness temperature and Globcover biome structures (technical note for the ATSR QWG).